Analysis Methods for Discontinuous Fiber Composites

Brian Head

A thesis

Submitted in partial fulfillment of the

Requirements for the degree of

Master of Science in Mechanical Engineering

University of Washington

2013

Committee:

Mark Tuttle

Paolo Feraboli

Ramulu Mamidala

Program Authorized to Offer Degree:

Mechanical Engineering

Abstract:
The mechanical performance of a Discontinuous Fiber Composite (DFC) material system called HexMC® is considered in this study. Specifically, the goals of the study were to 1) Predict the buckling and failure loads of three sizes of HexMC® angle beams loaded in pure bending. 2) Develop a stochastic modeling method that captures both the stiffness variation and membrane bending coupling effects exhibited by HexMC, and 3) Predict displacements and failure loads of a HexMC® brace with complex geometry subjected to two different loading conditions. The B-range of in-plane isotropic elastic properties was defined during the study. Measured buckling and failure loads of small and large size angles were subsequently predicted to within 16-22% and 18-32%, respectively, based on the B-range in elastic properties. Failure loads of medium size angles that did not buckle prior to fracture were predicted to within 2-14%. A stochastic modeling approach called the Random Laminate Volume Element (RLVE) method was also developed. The RLVE approach greatly improved buckling predictions for the small angles, but had little impact on predictions for the large angles size. Finally, the brace was modeled using the B-range isotropic properties. For the first load case, an FE analysis based on geometrically linear displacements, predicted failure to within 15% if failure occurred away from bolted regions. However when failure occurred near bolted regions the complex stress state in these regions made failure predictions inaccurate, since the actual out-of-plane elastic properties of HexMC® were not used during the FEA analyses. For the second load case, a geometrically nonlinear FE analysis predicted displacements well. However, severe stress concentrations at the failure location rendered the gross section strength values unusable, as measured and predicted strain levels far exceeded the nominal failure strain suggested by failure strength and in-plane modulus.

Table of Contents

List of Figures

List of Tables

1. INTRODUCTION

Composite materials are growing ever more popular. They are currently seeing increased use in the automotive, energy, and aerospace sectors. Specifically, within the aerospace sector composites have seen increased use, due to several of their beneficial properties. Probably the most influential of these is their specific properties. Properties such as specific strength and specific modulus allow manufactures to make lighter stronger parts, making airplanes more efficient than ever. The most recent milestone for composites in the aerospace industry is the first commercial flight of the Boeing 787 Dreamliner. The 787's primary structures are over 50% by weight composites [1]. By volume the fraction is obviously much higher than that. This use of composites in addition to other factors help the 787 to be the most efficient plane in its class, using 20% less fuel than any other plane of its size [2].

The primary types of composites used in the aerospace industry are continuous fiber laminates. These laminates have many attributes that make them ideal for most applications. For example, the anisotropy of the individual lamina allow for directional properties of a laminate to be tailored to specific applications. They also have a few drawbacks. For example, the individual layers, called plies, must be laid in specific orientations in most applications, much of the time by hand. This assembly of layers is costly. Additionally, producing complex curves can be difficult because the initially flat plies often have poor drapability (special weaves can exhibit superior drapbabilities and are often used in these cases). As another example, most materials used in the aerospace industry require curing in heated and pressurized ovens called autoclaves. These

autoclaves are expensive to operate, have long cycle times, and have relatively small volumes, making mass production of parts slow and costly. In cases where the strength and stiffness requirements of a part are not as critical, the cost of continuous fiber composites may not be justifiable.

A class of composites that may be suitable for these latter cases is Short Fiber Composites (SFCs). The most common forms of SFCs are Bulk Molding Compound (BMC) and Sheet Molding Compound (SMC). These typically consist of short glass fibers, less than 2.5 cm for BMC and between 2.5 and 7.5 cm for SMC. The fibers reinforce a matrix, typically a thermoplastic resin. The reinforcement improves stiffness and strength greatly over unreinforced resin. Parts can be produced by compression or injection molding with these compounds, resulting in a relatively fast manufacturing process at low cost [3]. In addition to these manufacturing advantages, SFCs also exhibit relatively isotropic material properties, which can be beneficial in many situations. These materials have been commercially available for many years. Work by Halpin and Pagano [4 , 5] in the late 1960's showed that the elastic properties of SFCs could be reasonably well-predicted. Historically however, SFCs have not been used in applications where strength and stiffness are of critical importance. That is, in the aerospace industry SFCs have been not been used in primary load-bearing structures.

More recently, a new class of high performance pre-preg-based SFCs have been developed with substantially-improved in-plane stiffness and strength compared to older systems. These new materials will be called Discontinuous Fiber Composites (DFCs) in this report, to distinguish them from the older SFC systems.

DFCs consist of chips of carbon fiber pre-preg randomly oriented in mats. There are a few commercial examples of these materials, one of which is HexMC® which is produced by Hexcel. Parts made using DFCs are typically produced using relatively low-cost and rapid compression molding processes. Aside from the ease of manufacturing, these DFCs have several qualities that make them excellent choices for some applications. They have been shown to exhibit modulus nearly as high as the equivalent quasi-isotropic layup based on continuous fibers [6], and they exhibit excellent notch insensitivity [7]. Because of these superior properties DFCs have been used in load-bearing structures in modern aircraft. For example, the window frames in the Boeing 787 are produced from HexMC® [8]. While these materials are now being used in load bearing applications, their use has been thus far limited by the lack of established analysis methods. The random nature of the chip orientation in DFCs makes predictions difficult, resulting in an expensive and tedious design process involving more testing than is necessary for more traditional laminates. The benefits gained by manufacturing ease, are reduced by the intensive design process. Additionally, the marginal benefits of choosing a DFC for a specific application are reduced, if the part ends up overdesigned, using more material, and weighing more than necessary. With the improvement of analysis methods, DFCs could find their way into more and more applications.

1.1. Study Objective and Tasks

The objective of this study was to establish best practices for modeling parts produced using a model DFC, namely HexMC®. The intent was to build on earlier work in this area [6 , 7 , 9 , 10 , 11 , 12, 13]. Previous efforts have focused on coupon level modulus and

strength and geometrically linear, elastic testing of HexMC® angle beams. In contrast, this work focused on specimens with more complex geometries subjected to loads high enough to cause nonlinear buckling/crippling conditions. The three main specific tasks were:

Task 1: Predict the buckling and failure loads of three sizes of HexMC® angle beams loaded in pure bending.

Task 2: Develop a stochastic modeling method that captures both the stiffness variation and membrane bending coupling effects exhibited by HexMC®.

Task 3: Predict displacements and failure loads of a HexMC® brace with complex geometry subjected to two different loading conditions.

2. LITERATURE REVIEW

2.1. Analysis Techniques for Discontinuous Fiber Composites

2.1.1. Modulus Estimation

There has been much work done to predict the behavior of SFCs. Halpin did early work predicting the modulus of SFCs [4] and Halpin and Pagano developed a laminate analogy for predicting the elastic properties of SFCs in 1968, which serves as the basis for the stochastic method that will be presented in Section 4 [5]. Their work established methods of approximating SFCs as symmetric laminates with volume fractions and stacking sequences chosen such that they match the volume fraction of fibers in various directions in the SFC. However, their work was based on traditional SFCs involving short individual fibers. In contrast, for the DFC material considered in this study (HexMC®) fibers within a chip are aligned locally, even though chip orientations are randomly. Using a method termed the Stochastic Laminate Analogy (SLA), Feraboli et al. developed a Monte Carlo simulation to predict the effect of randomly oriented chips of fibers, as opposed to the randomly oriented individual fibers studied by Halpin and Pagano [9, 13]. Their approach stochastically assigned chip fractions to Random Representative Volume Elements (RRVEs). When the chip fractions accumulated to the proper volume of the RRVE, a symmetric stacking sequence was specified that matched the fraction of fibers in each of a few distinct fiber orientations allowed. Then classical lamination theory was used to calculate the effective elastic properties, E_x, E_y, and υ_{xy} [9].

While this approach was successful in predicting the modulus variation measured on the surface of DFC coupon specimens, the method was less successful in predicting the behavior of more complex structures such as HexMC® angle beams. It is suspected that the discrepancies in these latter cases may have occurred because symmetric stacking sequences were assumed. This assumption is relaxed in this study. That is, the Monte Carlo approach initiated by Feraboli et al is extended in the present study to allow for non-symmetric stacking sequences. .

Since DFC composite structures are usually produced using compression molding, chips may become aligned due to flow, which would invalidate the transversely-isotropic nature of DFCs. Flow has been shown to have a large effect on material properties when flow is too great. In extreme cases the modulus was shown by Shifman to vary by as much as 300%, where flow was exceptionally high. [11]. Because of the extreme variation in modulus possible, the conclusion drawn by Shifman was that part molds should be designed to eliminate or reduce high flow regions and as such regions with high matrix flow are not a focus of this study. Shifman was also able to show that for parts where flow is limited, the elastic behavior of HexMC® angle beams subject to pure bending could be reasonably well-predicted using moduli measured during uniaxial coupon tension tests [11].

2.1.2. Strength Estimation

Feraboli et al. used the SLA to predict failure of HexMC®, but found that strength was under predicted [13]. This was at least partly due to the dependency on mesh size

exhibited by the RRVE modeling method, but may also be related to local stress concentrations exhibited by HexMC®.

2.2. Digital Image Correlation

Digital Image Correlation (DIC) is an optical technique for measuring displacements, shape or motion on the surface of a test specimen. A surface of a specimen is covered with a non-repetitive, random, and isotropic speckle pattern. During the test, the speckled surface of the specimen is photographed by one or two cameras on some time interval. If one camera is used, only in plane displacements can be measured, if two cameras are used, fully three dimensional displacements of the surface being observed can measured.

2.2.1. Basic Theory

DIC is conceptually very simple. The camera or cameras capture images of the surface throughout a test. During post processing, the software compares every image taken to the declared reference image. The software computes how far points on the surface have moved for each image. Once every point has been tracked in a specific image, then displacement fields in the two-dimensional plane perpendicular to the camera are known. If two cameras are used, displacements in three dimensional space are known. Once the displacement field(s) is known, strains are calculated by taking the derivative of displacements. Regardless of whether one or two cameras were used, only strain in the plane of the surface observed can be calculated. That is, DIC cannot be used to infer any component of the out-of-plane strain fields.

2.2.2. Application of Speckle Pattern

The application of speckle patterns is nearly as much of an art as it is a science. Ideally speckles are non-repetitive, isotropic, uniformly sized and of high contrast [14]. Speckles must be non-repetitive so that the camera(s) can tell different points apart. Speckle pattern must be isotropic, meaning that there should be no discernible direction to the speckles, which prevents directionality of results. Speckles should be uniformly sized, because speckles smaller than the ideal size will blur the image, and larger will create regions lacking distinguishing features. Lastly speckles should be high contrast, so that divisions between speckles and background are as sharp as possible.

The number of methods that can be used to apply speckle patterns is limited only by the user's imagination. Popular methods include painting with canned spray paint or an airbrush, or printing a speckle pattern on a sheet of paper and subsequently applying with an adhesive. Figures 1 through 3 show example speckle patterns produced using each of the methods.

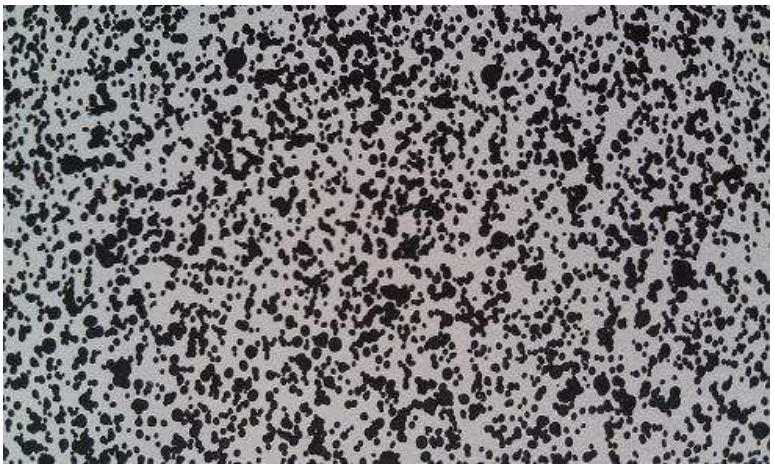

Figure 1: Spray Painted Speckle Pattern

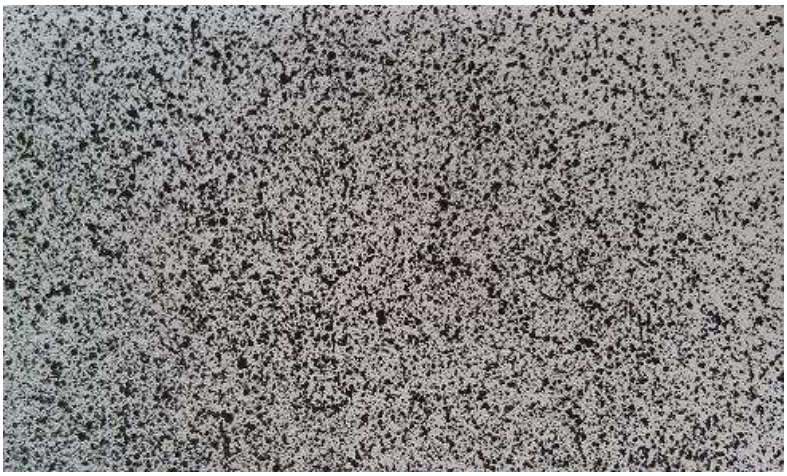

Figure 2: Air Brushed Speckle Pattern

Figure 3: Printed Speckle Pattern

Ideally speckles should be 3-5 pixels wide in the images taken by the DIC cameras [14]. Larger speckles provide no marginal benefit, and the minimum size of a subset increases. Smaller speckles result in aliasing problems. When the software determines where a speckle is, it tries to find the speckles center. If the speckle is too small, the center of the speckle can shift a large percentage of its size due to fluctuations in the image, causing large errors.

2.2.3. Reduction of DIC Data

While in theory image correlation is a simple process, in practice it is less straightforward. Several correlation parameters can have large impacts on the results obtained, and must be studied and understood. Errant results are easily obtained if the user is not familiar with the various parameters. In reality the software does not track individual speckles, but rather groups of speckles contained in subsets [14]. A single speckle is indistinguishable from its neighbors. The software actually tracks subsets of the image. The size of the subset is determined by the quality of the speckle pattern. In the author's experience, the smallest satisfactory subset is around 20 by 20 pixels. The subset size should be chosen such that each subset is distinguishable from other subsets [15]. In theory this requires containing at least 3 distinct speckles [14]. The larger the subset size, the more accurately position of that subset is tracked, but spatial resolution around the edges of the specimen is lost because displacements can only be correlated to within one half of the subset size of the edge of the specimen. In situations where data is desired near a hole or crack tip the smallest possible subset size must be used.

A second important parameter is how many pixels the software shifts over before choosing the next subset size. The software does not just break the surface into subsets, but rather subsets overlap. This step size can have a large impact on calculated strains. If the step size is too small, large numerical errors can occur leading to very noisy strains, and analysis time increases. If step size is increased, correlation of the images is faster and smoother strain results are obtained, however spatial resolution is lost, especially in regions of high strain gradients.

The last of the major parameters of importance is the filter size. The software filters the strains calculated by the derivative of the displacements. The size of this filter must be chosen carefully because it can smooth calculated strains, but once again risks filtering out fidelity in regions of high strain gradients.

2.3. HexMC® Properties

This section lists the nominal HexMC® properties that are used for the modeling to be reported in following sections. These properties were provided in a proprietary Hexcel report [16]. Table 2 and Table 3 list the nominal moduli and strengths, respectively.

Table 2: Nominal HexMC® Elastic Properties

In Plane Property	Value
Un-notched Tension Modulus	45.60 GPa (6.616 Msi)
Un-notched Compression Modulus	43.51 GPa (6.314 Msi)
Poisson's Ratio	0.322

Table 3: Nominal HexMC® Strengths

In Plane Property	Value	Type
Strength in Compression	346 MPa (50.2 ksi)	B-Basis
	393 MPa (57.0 ksi)	Average
Strength in Tension	277 MPa (40.2 ksi)	B-Basis
	344 MPa (49.9 ksi)	Average

As explained later, some of the analysis performed during this study were based on properties that differ from those listed here.

3. Isotropic Properties Modeling of Angle Beams

3.1. Nominal Dimensions

Three sizes of angle beams were produced for this study by the Hexcel Corporation. They were compression molding from HexMC®, a DFC produced by the Hexcel Corporation. HexMC® consists of chips of AS4/8552R pre-preg that are nominally 7.6 mm x 50.8 mm (0.3 in x 2 in). Figure 4 shows the three sizes of angles as received. Upon receipt, the beams were machined to 35.6 cm (14 in) in length.

Figure 4: Angle Beams as Received [11]

The large and medium angle sizes have the same nominal flange thickness of 4.8 mm (0.188 in) and flange lengths of 89 mm (3.5 in) and 64 mm (2.5 in) respectively. The small angle size has a nominal flange thickness of 2.5 mm (0.097 in) and flange length of

43 mm (1.7 in) respectively. Table 4 summarizes the angle sizes and cross sectional properties and Figure 5 shows the measurement locations for the angle dimensions.

Table 4: Nominal Angle Cross Sectional Properties

Flange length, *f* mm (in)	Flange thickness, *t* mm (in)	Major mom of inertia, I_z cm^4 (in^4)	Minor mom of inertia, I_y cm^4 (in^4)
89 (3.50)	4.8 (0.188)	52.0 (1.25)	22.9 (0.550)
89 (2.52)	4.8 (0.188)	32.0 (0.77)	7.74 (0.186)
43 (1.73)	2.5 (0.097)	5.41 (0.13)	1.29 (0.031)

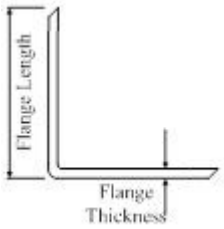

Figure 5: Angle Cross Section [11]

3.2. Measured Dimensions

The flange thicknesses of all angle beams tested were measured after the angles were tested. To obtain the average actual thickness of each size of angle, the thickness of every specimen tested was measured in four places. The average of those four measurements was taken to be the average for that specimen. The average thickness was taken to be the average thickness of every specimen of that size. The average thickness of every specimen can be found in Table 5. Additionally the thicknesses of two specimens of each

size were measured in 36 locations, 18 on each flange. The two specimens chosen were the two specimens that exhibited the lowest and highest failure moments for that size. Figure 6 shows the measurement locations on a medium angle beam. The crosses indicate measurement points. In cases where the measurement point fell on a fracture location, the thickness at that point was interpolated from surrounding thicknesses. Table 6 shows the summary of the thickness measurements for the angles

Table 5: Thickness Measurement Summary

Small		Medium		Large	
Specimen	Thickness mm (in)	Specimen	Thickness mm (in)	Specimen	Thickness mm (in)
S1	2.4 (0.095)	M2	4.75 (0.187)	L1	4.57 (0.180)
S2	2.4 (0.097)	M3	4.88 (0.192)	L2	4.68 (0.184)
S3	2.4 (0.095)	M4	4.71 (0.185)	L3	4.57 (0.180)
S4	2.4 (0.095)	M5	4.88 (0.192)	L4	4.45(0.175)
S5	2.4 (0.095)	M6	4.75 (0.187)	L5	4.70 (0.185)
--	--	M7	4.71 (0.185)	--	--
Average	2.42 (.095)	Average	4.76 (0.187)	Average	4.59 (0.181)

Figure 6: Medium Beam Sections

Table 6 shows the minimum, average and maximum measured thickness for both specimens of each size. In general the thickness varied linearly in both the length direction as well as the flange direction. This indicates that the variation in thickness over a specimen is due to misalignment of the tools during the compression molding process.

Table 6: Angle Beam Measured Thicknesses

Specimen	Design Thickness mm (in)	Minimum Measured mm (in)	Average Measured mm (in)	Maximum Measured mm (in)	Maximum Variation
S1	2.5 (0.097)	2.36 (0.093)	2.42 (0.095)	2.49 (0.098)	2.98%
S3	2.5 (0.097)	2.39 (0.094)	2.41 (0.095)	2.46 (0.097)	2.09%
M5	4.8 (0.188)	4.75 (0.187)	4.87 (0.192)	4.98 (0.196)	2.56%
M7	4.8 (0.188)	4.57 (0.180)	4.71 (0.185)	4.80 (0.189)	2.85%
L1	4.8 (0.188)	4.34 (0.171)	4.56 (0.180)	4.70 (0.185)	4.85%
L3	4.8 (0.188)	4.42 (0.174)	4.58 (0.180)	4.70 (0.185)	3.45%

3.3. Test Setup and Fixture

In total 16 angles were tested; five each of the small and large sizes, and six of the medium size [11,12]. The angles were loaded in a four point bending fixture, subjecting them to a pure bending moment. One inch of each end of the angles was clamped in the fixture, leaving a 12 in span of the beam subjected to the moment. Figure 7 shows a large angle mounted in the test fixture, being loaded by the Instron test frame. The beams were loaded under constant rate displacement control until substantial failure occurred. During testing displacement of the test frame cross head and load applied were measured and

recorded. Applied bending moment was calculated using $M=P/2*d$ where P is the load applied and d is the distance between the two supports on one side. For the test frame used, d was 25.4 cm (10 in).

Figure 7: Angle Test Fixture

After testing was completed, two 12.7 mm (0.5 in) thick steel plates were mounted in the test frame. The plates mounted in the frame can be seen in Figure 8.

Figure 8: Rigid Angle

The frame was loaded to the maximum load experienced by any angle. Cross head displacement and load was recorded. Five duplicate tests were run. From these tests, the average compliance of the test fixture was determined to be 0.415 mm/kN ($7.37*10^{-5}$ in/lbf). Figure 9 shows the load displacement curve for one of the tests.

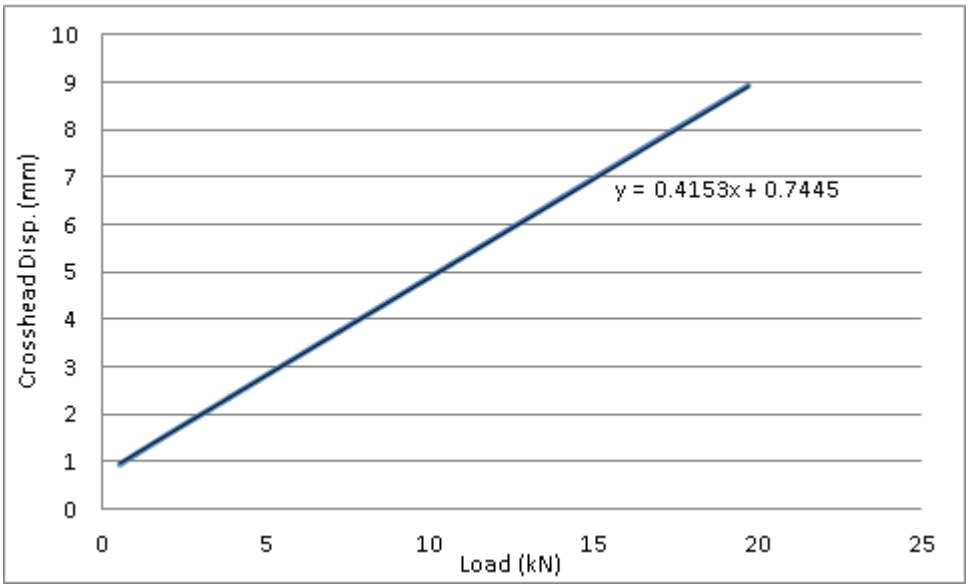

Figure 9: Fixture Compliance

Measured cross head displacements from the angle tests were then corrected for frame compliance to obtain the “rigid fixture” displacement. What the cross head displacement would have been, if the fixture was completely rigid. From the rigid frame displacement, the angular rotation of the ends of the beams was calculated based on the geometry of the frame. This allowed for comparison to models without having to model frame elasticity.

3.4. Modeling

The angles were modeled using FEMAP. FEMAP is a commercial pre and post processor for the NX Nastran finite element solver. The angles were modeled as eight noded

rectangular shell elements. The angles were modeled using both nominal thicknesses and using measured thicknesses. This allowed for the study of the effect of geometric variations on predicted buckling load. The beams were modeled as being 12 inches long. A rigid element was connected to all elements along the ends of each side of the beam. The rigid elements were fixed to a rigid element model of the frame. The cross beams were modeled as rigid beam elements and the vertical cross links were modeled using rod elements, with only axial and torsional stiffness. An enforced displacement was applied to the center of the top cross beam, and appropriate boundary conditions (BCs) were applied to the top and bottom cross beams. The model of the frame and a meshed medium angle including enforced displacement and BCs are shown in Figure 10.

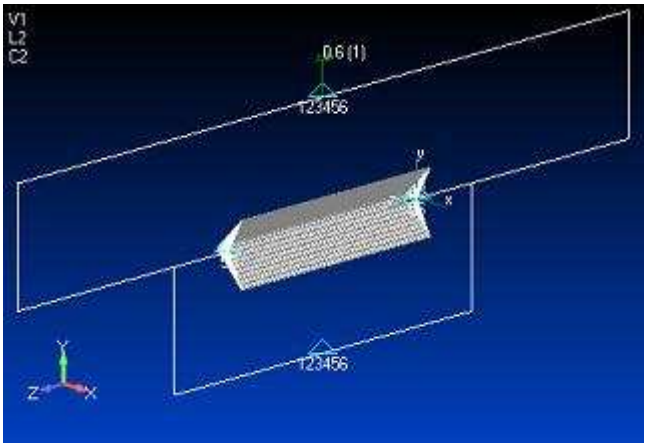

Figure 10: Medium Angle and Frame

The models were analyzed using NX Nastran's implicit Advanced Nonlinear Solution (SOL 601) [17]. The solution was divided into 50 steps. Each model 2-5 minutes to run. The angles were modeled using isotropic material properties, to evaluate the accuracy of predictions made by modeling the angles as isotropic. For buckling predictions, the compressive modulus was used, since the compressive flange governs buckling.

Consequently, the compressive modulus was used for failure predictions as well, since failure of buckled structures is largely dependent on the buckling load.

3.4.1. Isotropic Material Properties

Due to the random nature of DFC materials, they exhibit variations in modulus, both locally and over entire parts. Since buckling is highly dependent on modulus, the angles were modeled over a range in moduli. The range of moduli was calculated from proprietary test data provided by Hexcel [18]. The angles were modeled using the average modulus in compression, as well as a B-basis compressive modulus and what will be referred to as a B-max compressive modulus. The B-basis modulus is defined as the modulus over which 90% of samples fall 95% of the time. This same definition is used to define B-basis strength, as described in the CMH 17 Handbook [19]. Conversely, the B-max modulus is the upper bound on modulus. It is the modulus value under which 90% of the specimens fall 95% of the time. The measured moduli were assumed to be normally distributed and not structured during calculation of the B-basis and B-max values. Table 7 lists these calculated properties. A ±20% range of Poisson's ratio was also modeled to study the sensitivity to variations in Poisson's ratio.

Average strengths in compression and tension were used during failure predictions. While thickness specific strengths were reported, predicting failure with the average of the reported values resulted in better failure predictions on average. The average strengths used in failure prediction are listed in Table 77.

Table 7: Elastic Properties

In Plane Property	Value	Type
Un-notched compression Modulus	36.92 GPa (5.355 Msi)	B-Basis
	43.53 GPa (6.314 Msi)	Average
	50.14 GPa (7.274 Msi)	B-Max
Poisson's Ratio	0.258	Low
	0.322	Average
	0.386	High

Table 8: Failure Strengths

In Plane Property	Value MPa (ksi)	Type
Strength in Compression	346 (50.2)	B-Basis
	393 (57.0)	Average
Strength in Tension	277 (40.2)	B-Basis
	344 (49.9)	Average

3.4.2. Measured and Mapped Thicknesses

Two separate approaches were taken to model the angles with the measured thicknesses. First each angle size was modeled with the average measured thickness of all specimens of that size. The two specimens of each size were then modeled in 36 sections, with the measured thickness applied to each section. These two analyses were used to evaluate the relative effect of variations in thickness within a specimen compared to deviation from

average design thickness. Figures 11 through 13 show the thickness contours of all six angles that were mapped.

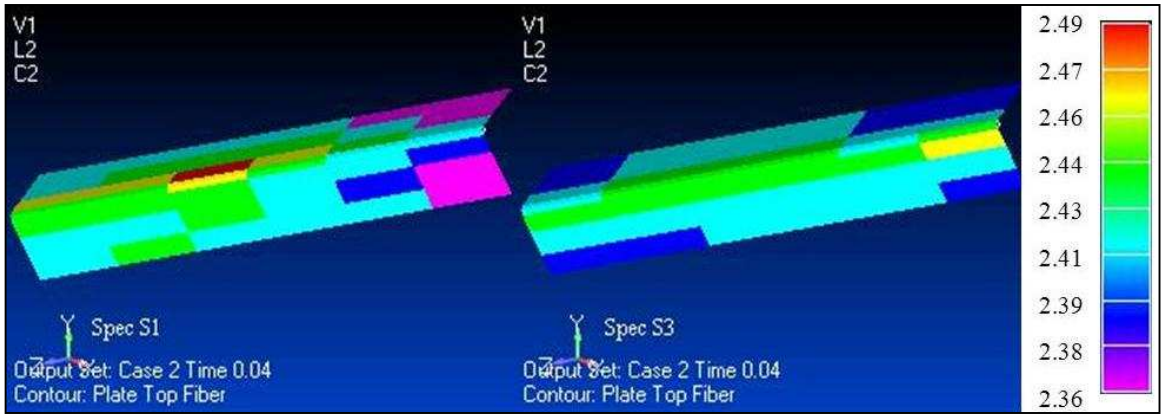

Figure 11: Small Angle Thickness Contours (mm)

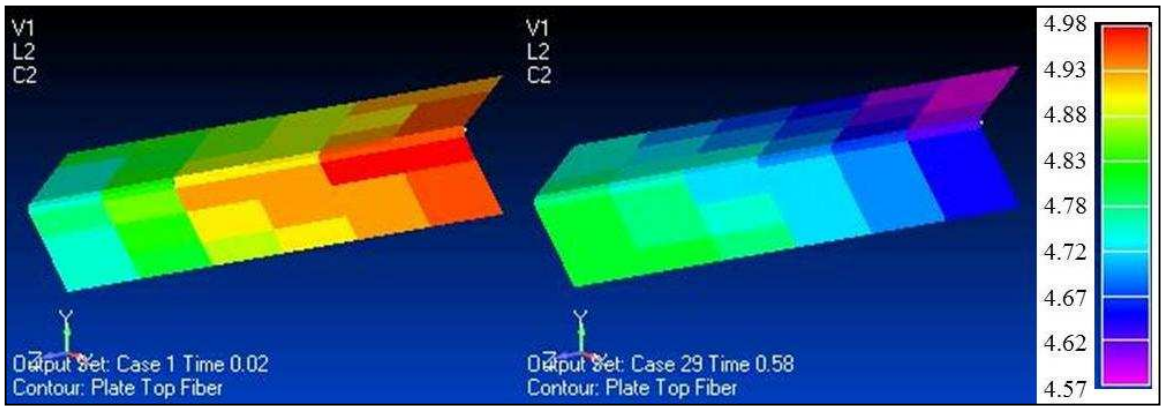

Figure 12: Medium Angle Thickness Contours (mm)

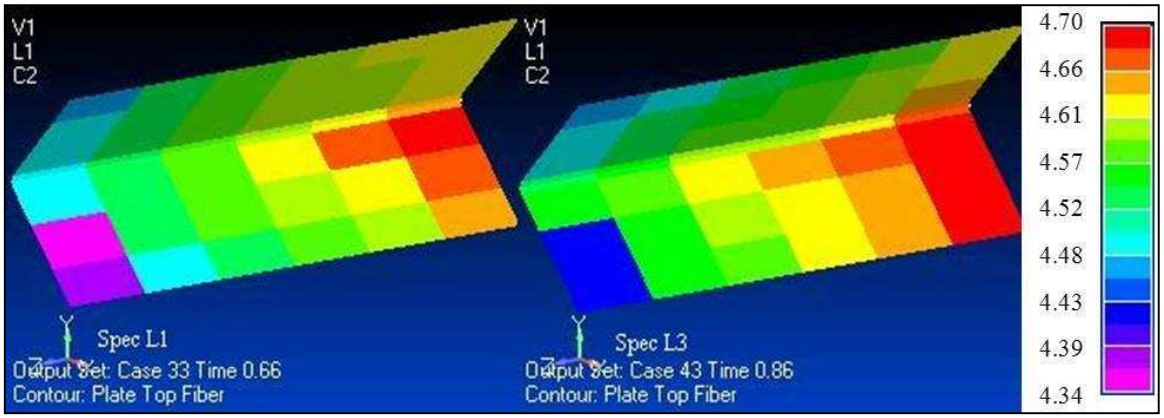

Figure 13: Large Angle Thickness Contours (mm)

3.4.3. Transverse Shear Properties

All previously reported modeling of HexMC structures have approximated the material as being fully isotropic. In reality, it is only approximately isotropic in-plane. The out-of-plane normal and shear moduli are much lower than the in-plane properties, because the randomized chips are oriented more-or-less in plane. The lower transverse shear modulus lowers the materials resistance to out-of-plane displacements, for example those present during a buckling response. The transverse shear modulus reported by Hexcel as measured by v-notched shear test (ASTM D7078) was 3.89 GPa (0.565 Msi) [16]. That is roughly 23.9% of the transverse shear modulus when calculated assuming the isotropic material properties listed in Table 7. The transverse shear modulus was not modeled over a range.

3.5. Experimental and Modeling Results

3.5.1. Testing Results

Five small and large angles and six medium angles were tested. Figures 14, 16 and 18 show the plots of the load versus cross head displacement for all specimens of all three angle sizes. After all the tests were completed, the measured displacements were corrected so that at zero load, the displacement was zero for each specimen. It is apparent that both the small and large angles undergo non-linear behavior, whereas the medium angle behaves fairly linearly until fracture. This agrees with what was observed during tests; the small and large angles visibly buckled, while the medium angle showed no visible buckling behavior before failure. For this study buckling will be defined by deviation from linear behavior by 5%, and failure strength is defined as the greatest load/moment supported by the angle at any point during the test.

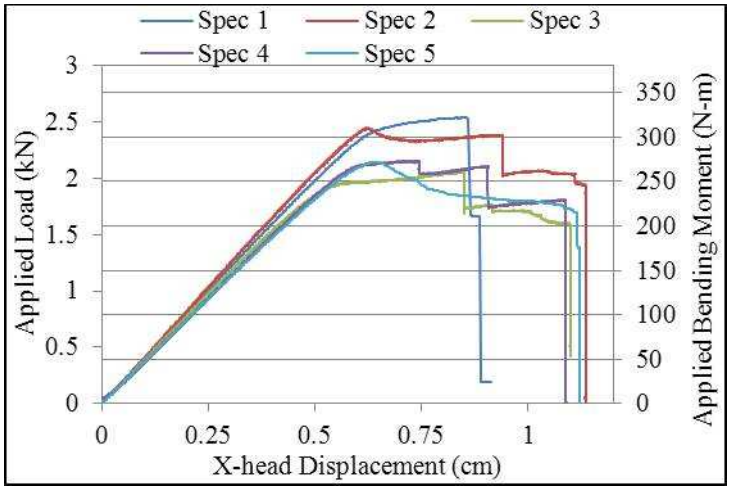

Figure 14: Small Angle Load Displacement Curves

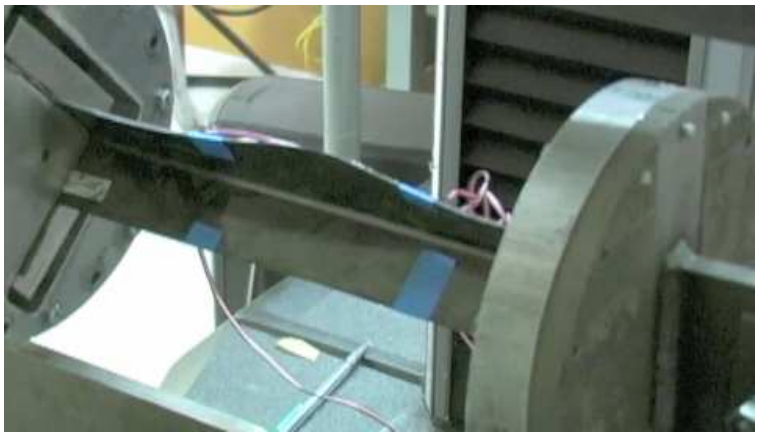

Figure 15: Spec S3 Pre-Failure

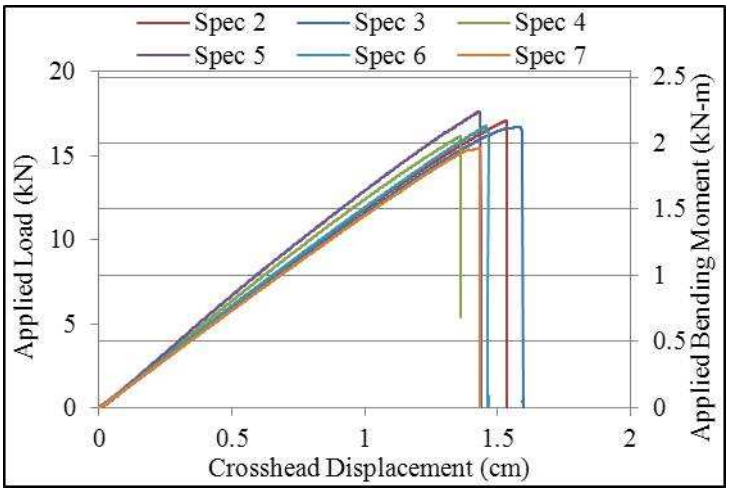

Figure 16: Medium Angle Load Displacement Curves

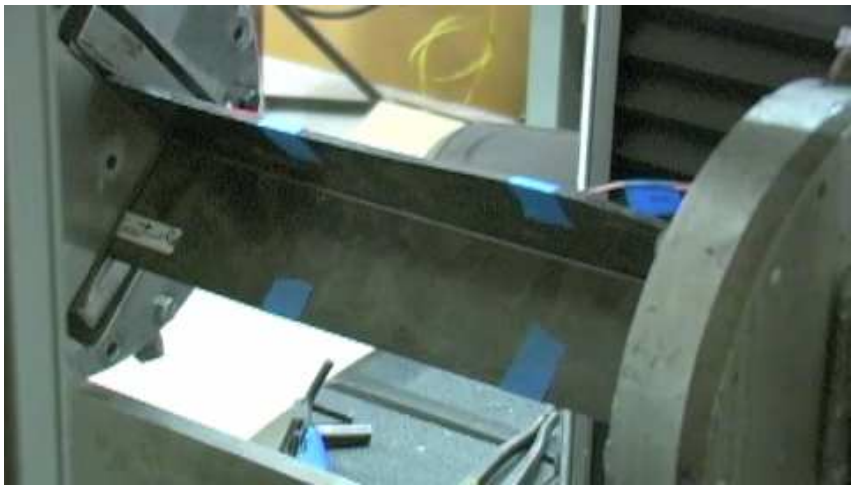

Figure 17: Spec M3 Pre-Failure

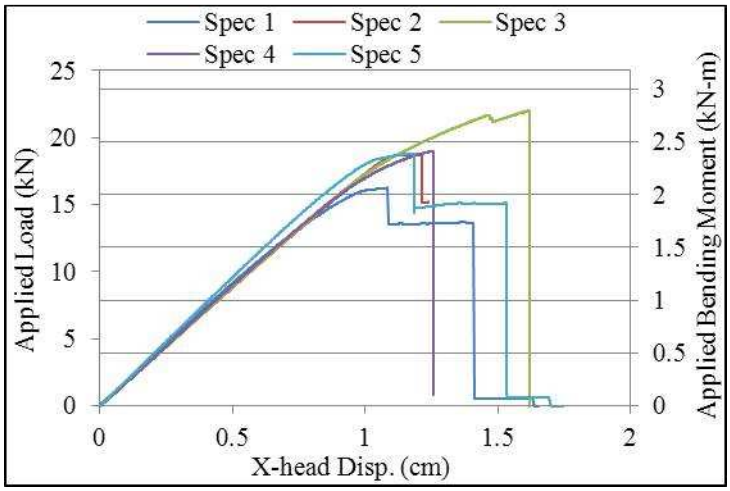

Figure 18: Large Angle Load Displacement Curves

The rotation of the ends of the angles was calculated from the displacement corrected for fixture compliance. End rotation is shown for all three angle sizes in Figures 19 through 21. Since the correction for fixture compliance is linear and only adjusts the displacement, the correction has no effect on buckling or failure loads, it only allows for

direct comparison to modeling. Table 9 lists the lowest, average and highest buckling and failure loads for all three angle sizes.

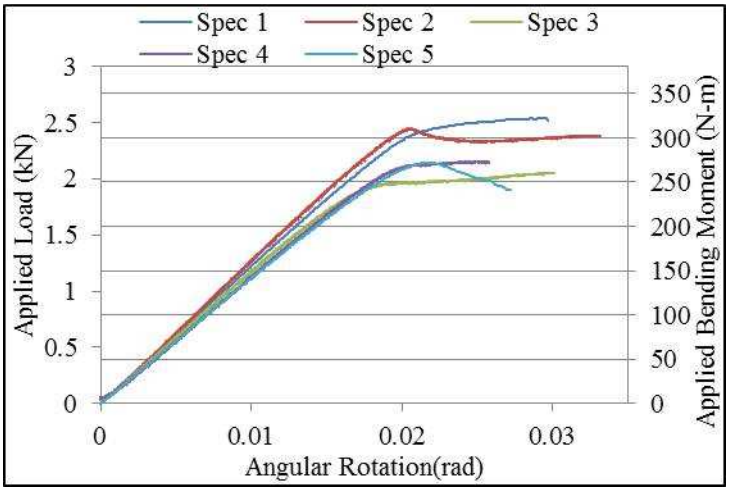

Figure 19: Small Angle End Rotation

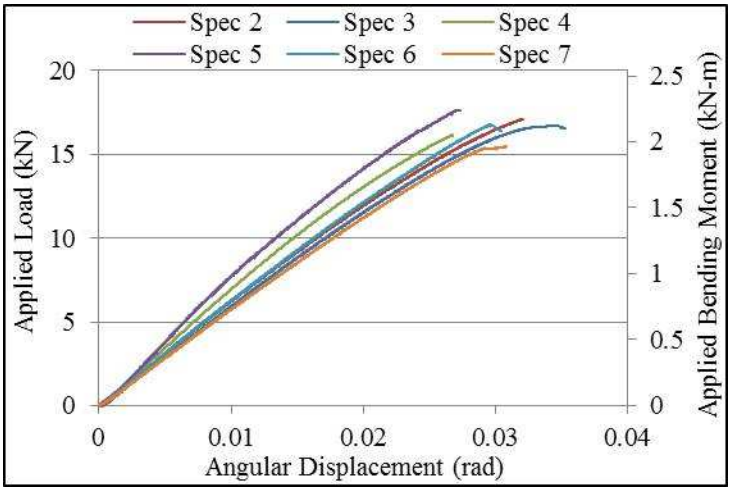

Figure 20: Medium Angle End Rotation

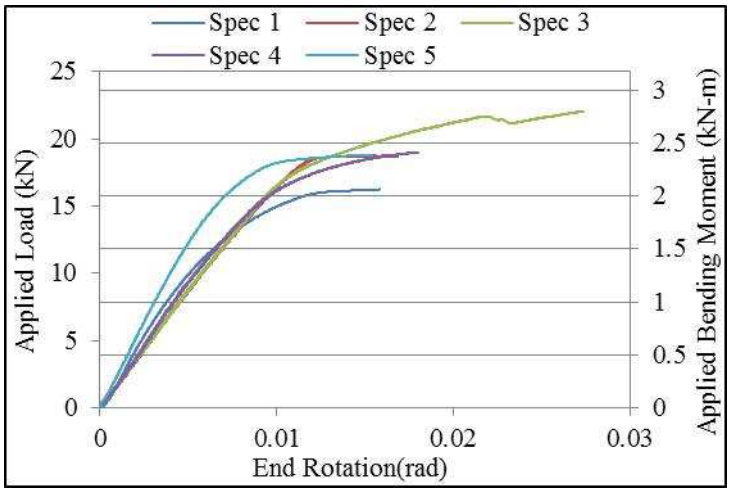

Figure 21: Large Angle End Rotation

Table 9: Angle Buckling and Failure Moments

		Buckling Moment N-m (in-lbf)	Failure Moment N-m (in-lbf)
Small Angle	Low	239 (2120)	261 (2310)
	Avg	277 (2450)	288 (2550)
	High	310 (2740)	322 (2850)
Medium Angle	Low	--	1962 (17,000)
	Avg	--	2114 (18,700)
	High	--	2242 (19,800)
Large Angle	Low	1757 (15,500)	2064 (18,300)
	Avg	2176 (19,300)	2400 (21,200)
	High	2367 (20,900)	2752 (24,400)

3.5.2. Modeling Results

Modulus Variation

The angles were first modeled based on nominal design thicknesses, using a range of modulus values. The results for all three angle sizes are presented in Figures 22 through 24. It can be seen that the small and large angles are predicted to exhibit non-linear behavior before failure, while in contrast the medium angle remains fairly linear until failure for the entire range of moduli. The predicted buckling loads, as calculated by 5% deviation, are listed in Table 9. The low, average and high buckling loads listed correspond to the angles modeled with the B-basis, average and B-max moduli, in compression respectively.

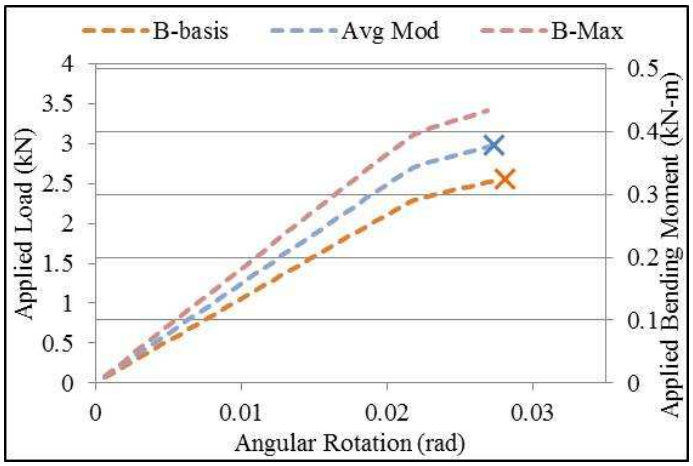

Figure 22: Small Angle Predicted Rotation

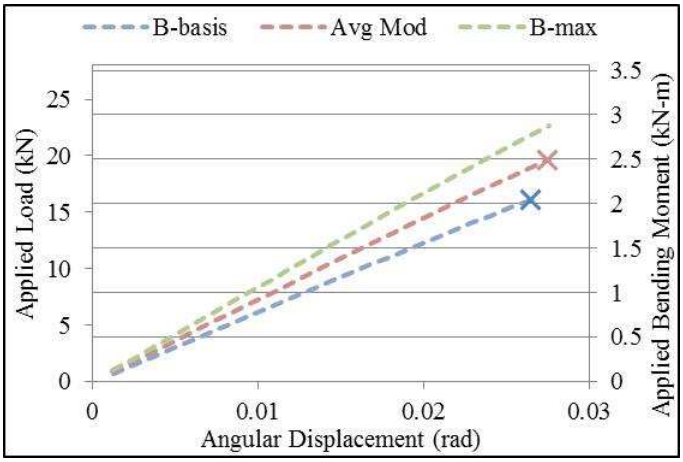

Figure 23: Medium Angle Predicted Rotation

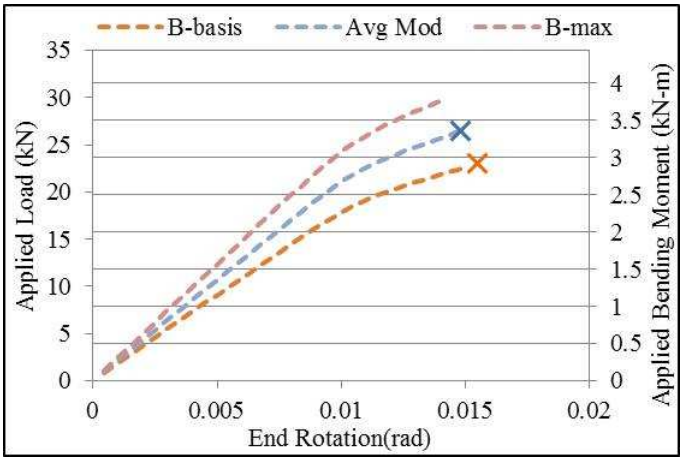

Figure 24: Large Angle Predicted Rotation

The failure moments of the beams were predicted using the B-basis and average strengths provided by Hexcel. A lower bound was defined as the moment at which the maximum or minimum stress in the model exceeded the B-basis strength in tension or compression respectively. The average failure load was calculated using the average modulus and strength. An upper bound on the failure load was not predicted, because no equivalent of B-max strength was available. The predicted failure loads are also listed in Table 9, and Figures 25 through 27 show the predicted stress contour of three angles at the time step

immediately after to the respective average predicted failure load. The B-basis and B-max moduli varied from the average modulus by ±15.2%. This variation in modulus caused a variation in predicted buckling load of ±15.2% on average over all three angles. If a Variation Sensitivity Parameter (VSP) is defined as the magnitude of the ratio of fractional change in predicted buckling load divided by the fractional change in the property that caused it, it can be seen that the angles have an average modulus VSP of 1.0.

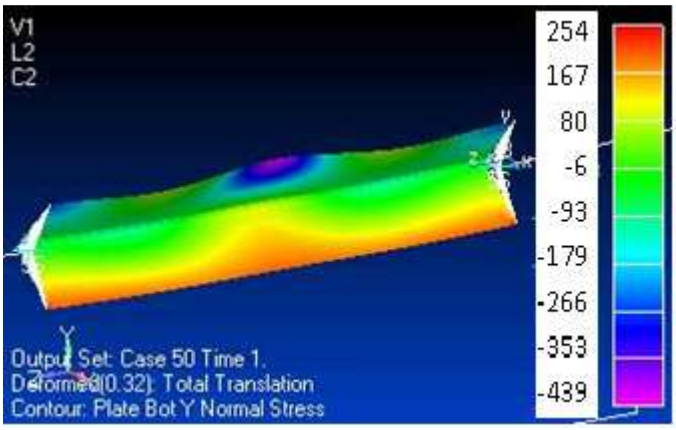

Figure 25: Predicted Small Angle Failure Stress Contour (kPa)

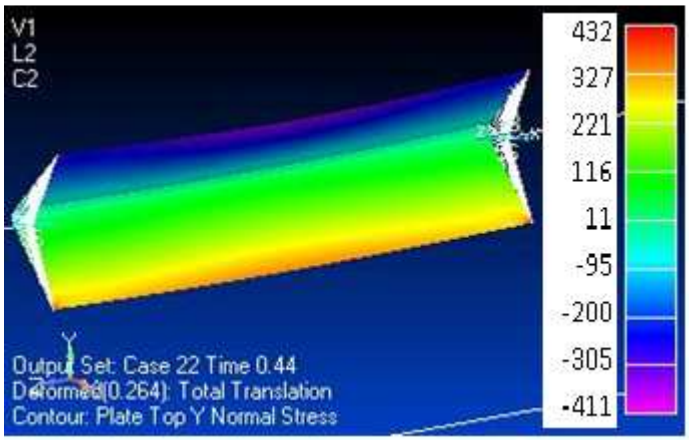

Figure 26: Predicted Medium Angle Failure Contour (kPa)

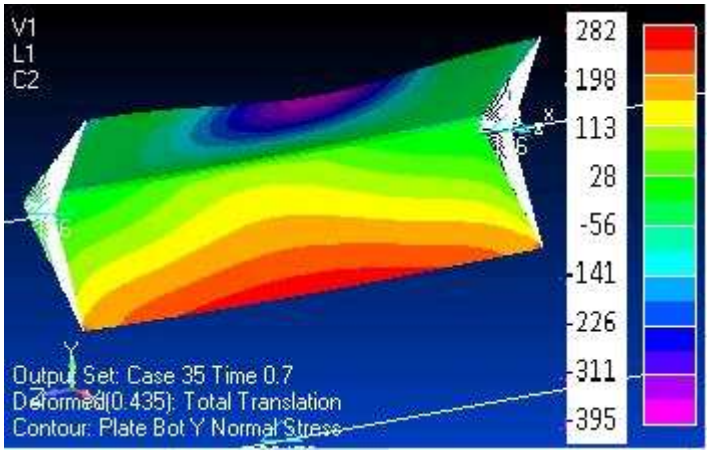

Figure 27: Predicted Large Angle Failure Contour (kPa)

Average Thickness Variation

To study effect of thickness variation, the angles were also modeled based on measured flange thicknesses. The thickness of every specimen tested was measured in four locations, two on each flange, using micrometers with ± 0.013 mm (0.0005 in) precision. The three angle sizes were modeled with the average measured thickness of all specimens of that size over the same range in moduli previously presented. The predicted failure and buckling moments from this study are listed in Table 9. In this table, the low, average and high represent the lowest, average and highest failure or buckling load respectively for experiments. For the buckling prediction, low, average and high are based on B-basis, average and B-max moduli respectively. For the failure prediction, low and average are based on B-basis strength and moduli, and average strength and moduli respectively.

Table 10: Buckling and Failure Prediction Comparison

		Buckling						Failure			
		Low		Average		High		Low		Average	
		Moment N-m (in-lbf)	Error %	Moment N-m (in-lbf)	Error %	Moment N-m (in-lbf)	Error %	Moment N-m (in-lbf)	Error %	Moment N-m (in-lbf)	Error %
Small Angle	Experiment	239 (2112)	--	277 (2451)	--	310 (2747)	--	261 (2307)	--	288 (2546)	--
	Design	302 (2675)	26.7%	356 (3155)	28.7%	411 (3634)	32.3%	325 (2880)	24.8%	379 (3358)	31.9%
	Measured Average Thickness	288 (2546)	20.5%	339 (3002)	22.4%	391 (3458)	25.9%	306 (2706)	17.3%	357 (3158)	24.0%
	Measured Average – Trans Shear	278 (2456)	16.3%	326 (2875)	17.3%	372 (3285)	19.6%	299 (2647)	14.7%	347 (3071)	20.6%
Med. Angle	Experiment	--	--	--	--	--	--	1960 (17350)	--	2114 (18707)	--
	Design	2293 (20298)	--	2704 (23934)	--	3111 (27535)	--	1962 (17366)	0.1%	2401 (21252)	13.6%
	Measured Average Thickness	2274 (20128)	--	2681 (23733)	--	3085 (27303)	--	1954 (17293)	-0.3%	2389 (21149)	13.1%
	Measured Average – Trans Shear	2177 (19222)	--	2544 (22460)	--	2902 (25620)	--	1993 (17109)	-1.4%	2343 (20738)	10.9%
Large Angle	Experiment	1757 (15550)	--	2176 (19256)	--	2367 (20949)	--	2063 (18260)	--	2410 (21330)	--
	Design	2450 (21685)	39.5%	2889 (25569)	32.8%	3328 (29457)	40.6%	2917 (25820)	41.4%	3364 (29776)	39.6%
	Measured Average Thickness	2197 (19448)	25.1%	2591 (22931)	19.1%	2985 (26418)	26.1%	2713 (24017)	31.5%	3115 (27568)	29.2%
	Measured Average – Trans Shear	2144 (18931)	21.7%	2515 (22207)	15.3%	2879 (25418)	21.3%	2695 (23854)	30.6%	3092 (27368)	28.3%

Table 11 shows the variation in thickness from design values, the change in predicted buckling load, and the corresponding thickness VSP for each angle size. By comparing the three, it can be seen that the angles have an average thickness VSP of 2.78.

Table 11: Effect of Thickness Variation

	Thickness Difference from Design	Buckling Load Variation	Thickness VSP
Small - 0.095 in	-1.7%	-4.9%	2.85
Medium - 0.187 in	-0.3%	-0.8%	2.77
Large - 0.181 in	-3.8%	-10.3%	2.73

An alternate method of accounting for flange thickness variations was the use of mapped thicknesses. In this case two specimens of each size were modeled in sections, with the measured thickness assigned to each section. The two specimens of each size were those that exhibited the lowest and highest buckling and failure moments. These mapped models were analyzed for only the average modulus in compression. Figures 28 through 30 show the effect of mapping the thickness for a specific angle compared to modeling the entire angle at the average thickness for one specimen of each size. In the case of the small and large angles, angle compliance and buckling load are clearly more effected by variation in average thickness than variation in local thickness over a single specimen. For the medium angles, there is hardly an effect before failure is predicted to occur around 2.4 kN-m (21,000 in-lbf).

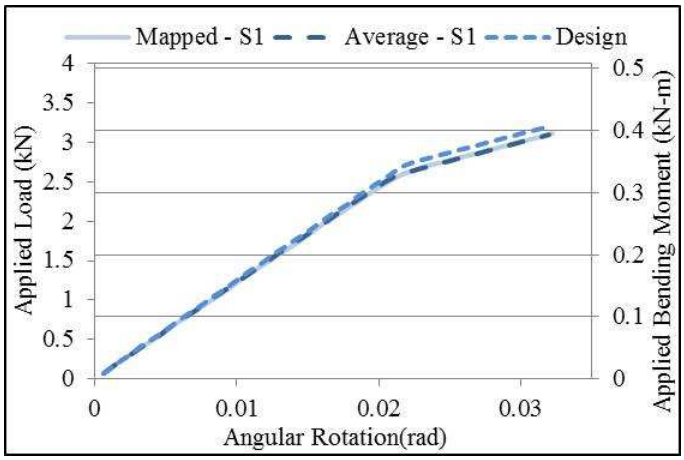

Figure 28: Small Angle Thickness Variation

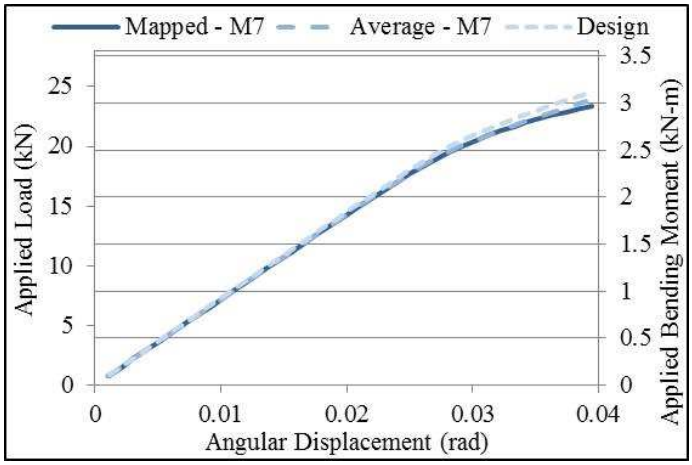

Figure 29: Medium Angle Thickness Variation

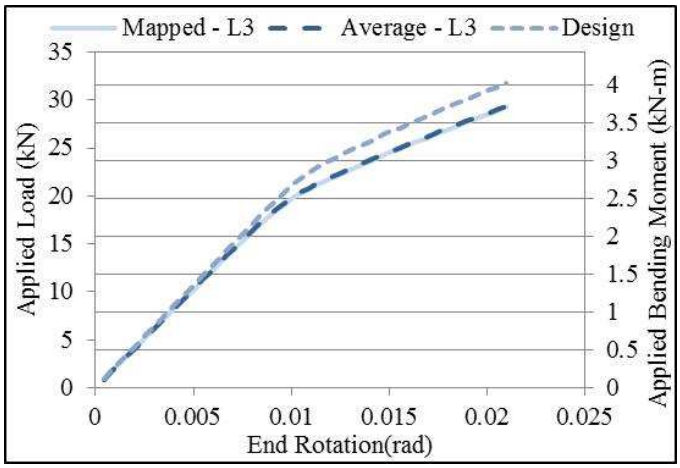

Figure 30: Large Angle Thickness Variation

Poisson's Ratio Variation

Poisson's ratio variation caused effectively no change in predicted buckling or failure load. The average Poisson's ratio VSP for the three angles was found to be less than 0.015.

Prediction vs. Measured

Table 9 lists the experimental failure and buckling loads as well as the predicted failure and buckling loads for the design thickness, average measured thickness and average thickness with transverse shear properties models. The results from the mapped thickness models are not presented as they do not vary significantly from the buckling and failure moments predicted by the average thickness models.

The average thickness models clearly provide better predictions of buckling and failure. Figures 31 through 33 show the moment vs. rotation plot for all three angles modeled using average measured thicknesses. The plots are of end rotation, calculated from the rigid frame displacement. It can be seen that the displacement of the angles is well

predicted and enveloped by the range of moduli modeled. The buckling and failure loads are over predicted in every case. For the small and large beams it can also be seen that the severity of the buckling behavior is not well predicted. The bending moments supported by the small and large specimens were nearly constant post-buckling, whereas the FEA models predict continued increase in load bearing post buckling. Table 9 shows the comparison between predicted and measured failure and buckling loads for the design thickness and average measured thickness models.

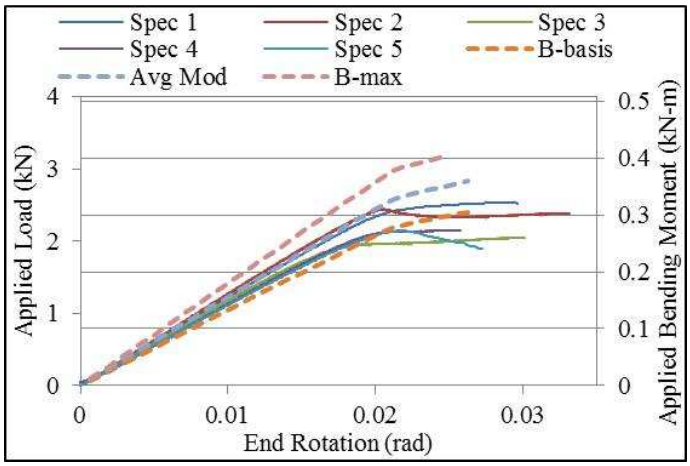

Figure 31: Small Angle Prediction Comparison

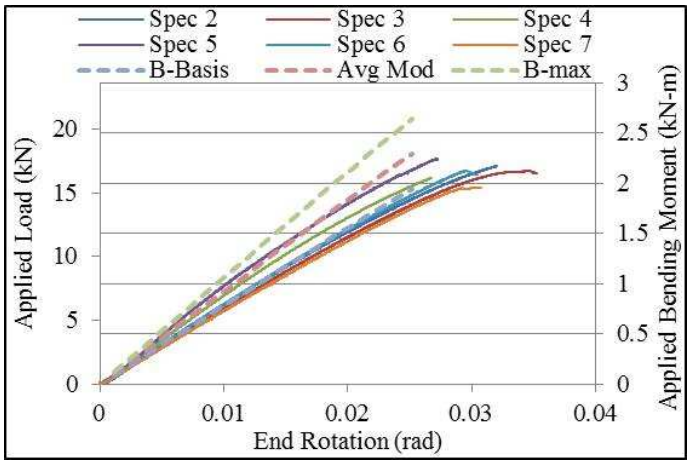

Figure 32: Medium Angle Prediction Comparison

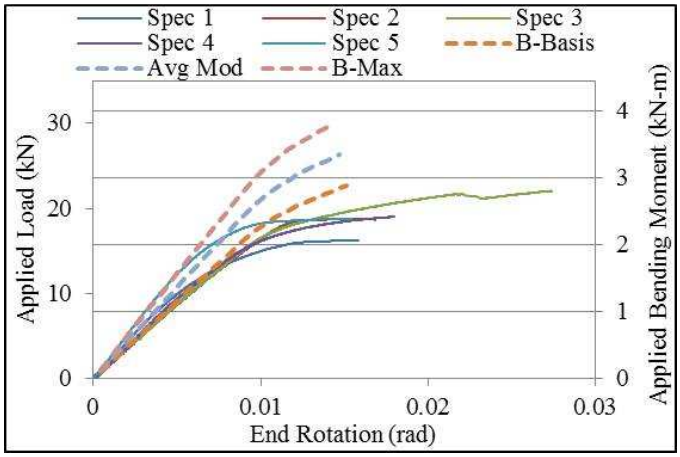

Figure 33: Large Angle Prediction Comparison

3.6. Discussion

3.6.1. Variation Sensitivity Parameters

The thickness VSP for the angles studies was 2.72. The variation of thickness from the design value has a great impact on performance of the angles. Hilburger and Starnes [20] reported a thickness VSP of 2 for crippling in orthotropic and quasi-isotropic graphite-epoxy composite shells. If the measured thickness of the angle flange is t, then the effective thickness, t_{eff}, is actually $t*\sqrt{2}$, where t_{eff} is the thickness of the flange parallel to the applied moment. When this is taken into account, for the angles tested the thickness VSP is 1.97, which varies from that reported by Starnes by only 1.5%. Thickness variation can have a large impact on buckling and consequently failure load for a small deviation from design thickness. However, produced parts can be easily tested for compliance with specified tolerances. This limits the variation in buckling behavior due to thickness effects to manageable and predictable levels.

The modulus VSP for the angles studied was 1.0. In the same study, Starnes reported a fiber fraction VSP of 2.7. Using classical lamination theory, and standard carbon fiber composite properties, a variation in fiber fraction of 3% causes a change of slightly less than 3% in modulus for the quasi-isotropic layup used by Starnes [20]. This indicates that modulus variation has a greater effect on the buckling load for the shells studied by Starnes than the angles studied here. With a VSP of 1.0, modulus variation has a relatively smaller effect for the same fractional variation However, as the material is produced with randomly oriented chips and the chips exhibit a large difference in

modulus between the one and two directions, the variation in modulus has the potential to be much larger than the variation in thickness. Feraboli et al showed that for the same HexMC® material, local strains on the surface of a tensile coupon can vary more than ±20 from the average [7]. The effect of this local (as opposed to the global variation modeled in this study) variation in modulus on buckling loads is discussed in Section 4.4. The Poisson's ratios VSP clearly shows that even large variations in Poisson's ratio have no substantial effect on buckling load of the angles subjected to pure bending.

3.6.2. Buckling and Failure Predictions

For the small and large angles the range in moduli modeled enveloped the range of pre-buckling displacements very well when the angles were modeled at average measured thicknesses. Predictions of the medium angles based on this same approach were reasonable, although displacement were slightly over predicted. The buckling loads for the small and large specimens were over predicted by an average of 18.2% and the lower bound buckling moment was over predicted by an average of 19%. The failure moment of the angles that experienced buckling was over predicted by an average of 25.6% and the lower bound was over predicted by an average of 24.8%, with the failure moment of the smaller angle being predicted about 10% better than for the large angle. This is due to the larger difference between buckling and failure moments for the large angles, combined with the poor prediction of post-buckling load bearing behavior. Failure of the medium angle, the only one not to buckle, was predicted much better. The average failure

moment was over predicted by only 14%, and the lower bound of failure was under predicted by only 2%.

It can be seen that modeling the angles at the average measured thickness and with actual transverse shear properties significantly improves the predictions of buckling loads versus modeling to design thickness. Additionally, based on the average variation over a single specimen the angles average variation from design thickness has a greater effect on agreement with experiments than thickness variation over a single specimen.

3.6.3. Improvement of Predictions

Several factors that impacted the accuracy of the buckling and failure predictions have the potential to be further addressed. First, in order to more accurately predict failure, both buckling load and post buckling load bearing behavior must be better predicted. If either of these are poorly predicted, an accurate failure prediction cannot be achieved. In order to better predict buckling load, there are a few avenues that should be explored. The first is local modulus variation. The effect of random, non-uniform modulus is unknown. In addition, not only modulus variation along the surface should be considered. Modulus variation through the thickness should also be considered. If the random oriented chips are not roughly symmetric through the surface, this could cause coupling terms in the stiffness matrix. These effects are explored in Section 4.4.

Another cause of buckling load variation could be localized failures, prior to failure and even the onset of buckling. During testing, audible cracks and pops were observed, before and after visible buckling in some cases. The structural effect of these micro-failures, if any, is unknown. Lastly, as with any buckling experiment, disparity between measurements and predictions is likely due to slight misalignment during test set-up. These misalignments are very hard to model, and could be the focus of future work.

4. Stochastic Random Layup Analysis

Previous work by Feraboli et al. [7] employed a variation on the laminate analogy for discontinuous fibers proposed by Halpin and Pagano [5]. The stochastic laminate analogy was shown to effectively predict the stiffness variation in DFC parts. However, the laminate analogy presupposes a symmetric stacking sequence (a quality not definitely exhibited by the random chip orientations). The presupposition of the symmetric stacking sequence eliminates the possibility for membrane-bending coupling effects. For most cases, the small out-of-plane displacements exhibited due to in plane loads are inconsequential for predicting the behavior of DFC parts. However, for some specific cases such as predicting buckling/crippling behavior, it is suspected this coupling could be the cause of some of the disagreement between the predicted and measured angle buckling results. This sections established a proposed a method for predicting both stiffness variation and out-of-plane displacements due to uniaxial tensile loads. The method is then applied to the prediction of buckling load of the angle beams.

4.1. Testing

To validate the proposed model and establish model parameters 18 tensile coupon specimens were tested in the elastic range. The specimens were cut from 330 mm x 457 mm (13 x 18 inch) flat plates produced from HexMC® by compression molding. Total specimen size was 330 mm x 38.1 mm (13 inches x 1.5 inches) wide. The specimens were tested in an Instron test frame to 87.6 MPa (12.7 ksi) at a displacement controlled rate of 0.5 mm/min (0.0197 in/min). With 50.8 mm (2 inches) gripped at each end, the total gauge length was 9 in. The specimens were gripped in grips with both the top and

bottom grips fully fixed. The specimens for each thickness came from two different plates, four plates total between the two thicknesses.

The specimens were covered with a speckle pattern produced by first painting them with an even coat of flat white spray paint followed by speckling with black spray paint. Figure 34 shows four speckled specimens of each thickness.

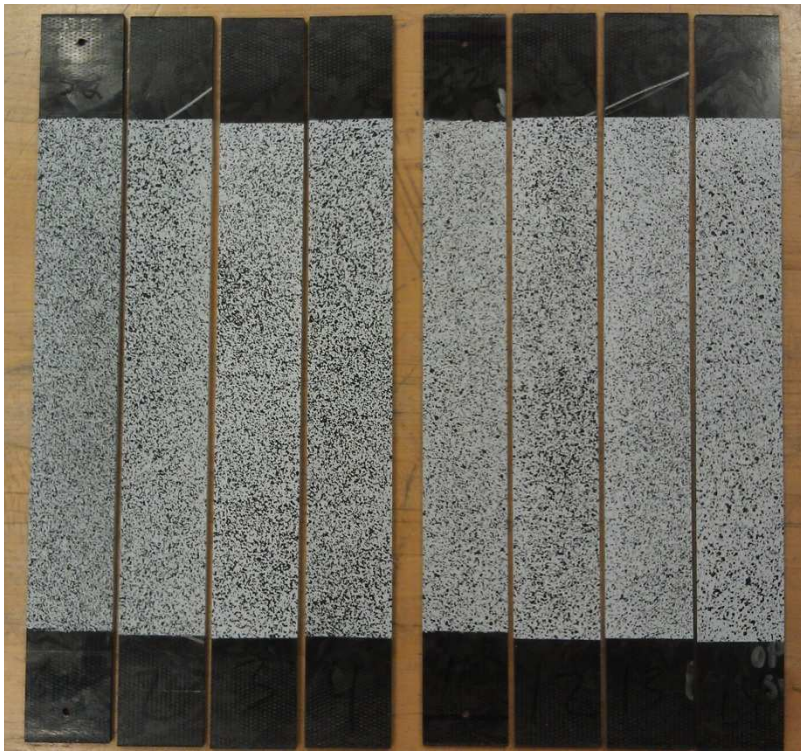

Figure 34: Speckled Specimens

A set of DIC images was taken every 1.3 seconds, giving on average 70 sets of pictures per test. In total, 20 tests were conducted. One specimen of each thickness was tested twice, where displacements on opposite surfaces were monitored. This allowed for evaluation of the validity of the out-of-plane displacement measurements, and average modulus measurement.

Displacement fields were measured with the use of VIC 3-D, a commercial Digital Image Correlation (DIC) system produced by Correlated Solutions Inc. By measuring full 3D displacement fields both in plane strains as well as out-of-plane displacements were measured.

4.2. Modeling

4.2.1. Method

In order to predict the out-of-plane displacements due to in plane loads, the model must capture the random orientation of the chips through the thickness of the material. Furthermore the random "stacking sequence" must vary from point to point across the surface of the material. To contrast, Feraboli's stochastic laminate analogy approach captures the variation over the surface, but neglects the random/non-symmetric layup through the thickness [7]. For practical reasons when doing the analysis, the layup cannot vary from point to point, but must vary by discrete finite regions which we will call Random Layup Volume Elements (RLVE). To accomplish this, a Visual Basic code was created which generates a FEMAP geometry model that is broken up into sections of a chosen size. Each section represents a single RLVE. For each RLVE the code steps through the layers, assigning each layer a random orientation. The randomly chosen orientations were allowed to vary continuously from 0 to 180 degrees. The layers are assigned anisotropic material properties. The properties assigned correspond to the properties of the precursor pre-preg for the HexMC® material. Table 12 lists the material properties for the AS4/8552R precursor material system used to produce HexMC® mats

[21]. The actual values used for modeling were adjusted to account for the resin content typically seen in HexMC® parts.

Table 12: Chip Properties in Tension

E_{11}	132 GPa (19.1 Msi)
E_{22}	9.23 GPa (1.34 Msi)
ν_{12}	.335
G_{12}	4.82 GPa (0.7 Msi)

The random orientation is generated with the Visual Basic function rnd.NextDouble. This process is repeated until the laminate is the proper thickness in that region, at which point the code generates a laminate property in FEMAP, and dictates FEMAP to mesh the RLVE with the user defined element size. The code then steps to the next RLVE. When the layup generation subroutine is finished, the model has a unique layup and property for each RLVE in the model and every RLVE is meshed. The code then dictates the generation of boundary conditions and loads. The model is analyzed using the FEMAP static solver and the average strain over several gauge regions and the maximum out-of-plane displacement is written to an Excel file before the model is closed and the program starts over. Each iteration takes 5-10 seconds to complete on a desktop computer.

4.2.2. Convergence

The number of runs required for the program to converge to an average modulus and out of place displacement is another important factor. Feraboli showed in [7] that for their program, the minimum, maximum and average predicted moduli converged after about

5000 runs. Figure 35 shows the maximum, minimum and running average of the modulus on the left hand vertical axis and the out-of-plane displacements respectively for a sample run on the right hand axis. This shows that both the predicted effective modulus as well as the average magnitude of the B-matrix terms have stabilized by 5,000 runs.

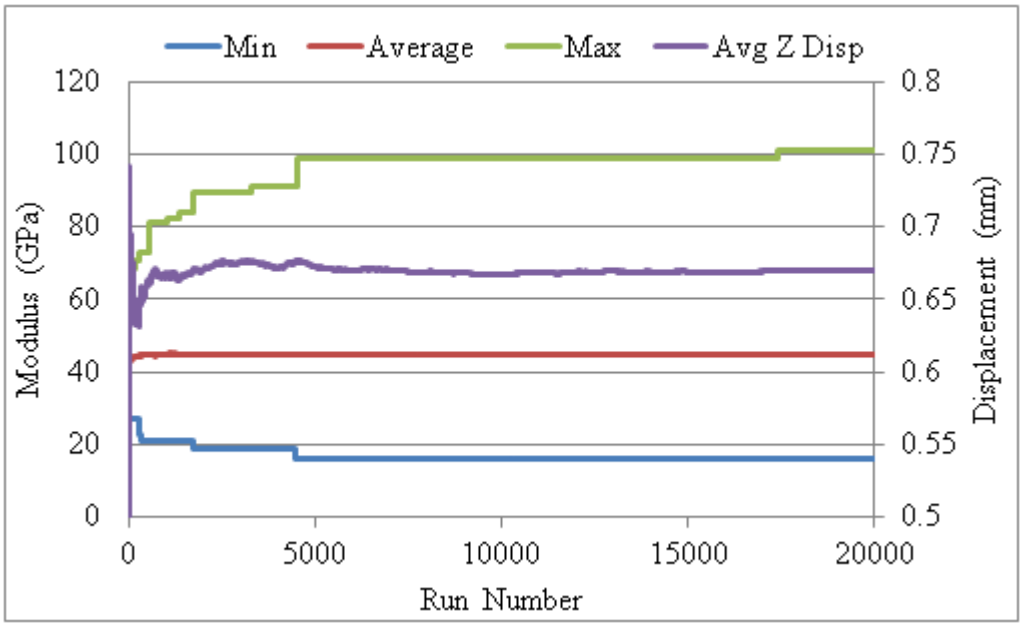

Figure 35: RLVE Model Convergence

4.2.3. Sensitivity Study

There were two major parameters that needed to be determined through sensitivity studies; the size of the RLVEs and the mesh size. Previous work by Feraboli [7] used an empirical comparison to determine the RRVE size to be 12.7 mm x 12.7 mm (0.5 inch x 0.5 inch). In their work, reasonable agreement between local and global stiffness variation predictions and measurements were achieved. However, since predicted out-of-plane displacements are also desired in this study, a combination of the variation in predicted stiffness and out-of-plane displacements was used to define the proper RLVE

size. The specimens were modeled with 6.35 mm, 12.7 mm and 19.1 mm (0.25 inch, 0.5 inch, and 0.75 inch) square RLVEs with hopes of interpolating between the predictions to the measured values for modulus variation, as well as average out-of-plane displacement and the variation in out-of-plane displacement. Ideally all three comparisons would predict the same RLVE size.

Mesh size was also investigated. It was found that for all RLVE sizes, mesh size had little impact on predicted average strain or out-of-plane displacements for three element sizes, 1.59 mm, 3.18 mm and 6.35 mm (0.0625 inch, 0.125 inch and 0.25inch) square elements. Table 13 shows the predicted average strain and max out-of-plane displacement for a single set of RLVEs, modeled with the three mesh sizes. It can be seen that even for such large changes in mesh size the predicted average strains and out-of-plane displacements vary by less than 1%.

Table 13: Global Strain Variation

Element Size	Avg Strain µin/in	Max Z Disp mm (in)
Small	2066.667	1.52 (0.0599)
Medium	2063.333	1.52 (0.0598)
Large	2055.556	1.51 (0.0595)

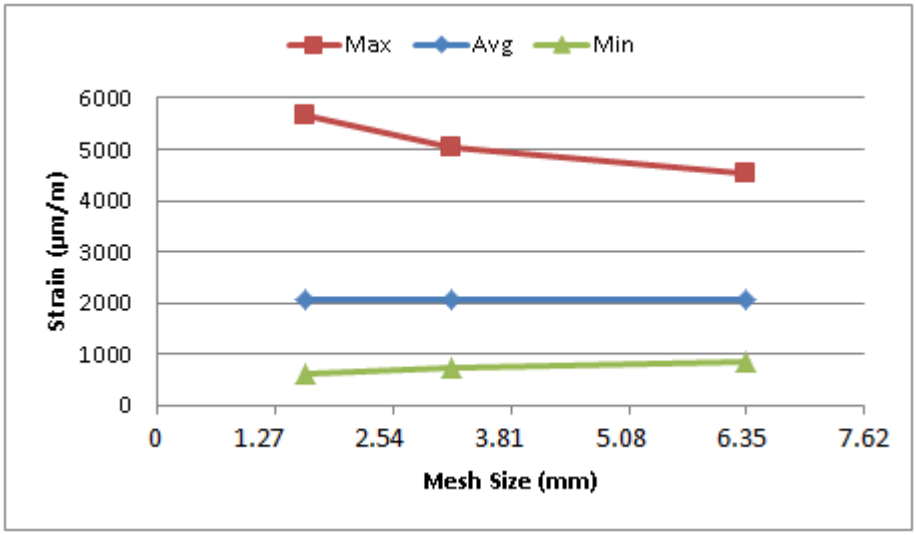

Figure 36: Local Strain Variation

Local strain variations on the other hand were found to be dependent on mesh size. Figure 36 shows the local maximum, average, and minimum strain for a sample model. Figures 37 through 39 show the same model analyzed with large medium and small elements respectively. It can be seen that as elements get small the boundaries between RLVEs become more distinct. The change in local strain variations seen by changing elements are not representative of actual behavior of the material being modeled, but rather singularities where the properties change discontinuously from one RLVE to the next. Because even the smallest modulus gauge region spans more than one of the largest modeled RLVEs, this effect is effectively washed out. For this reason, the median element size of 3.18 mm (0.125 inch) was chosen for all modeling.

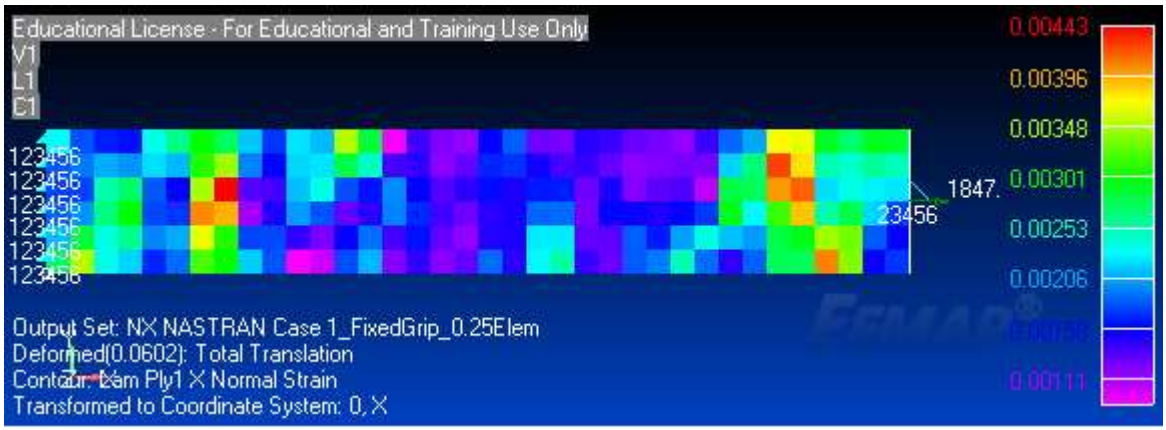

Figure 37: 6.35 mm (0.25 inch) Elements

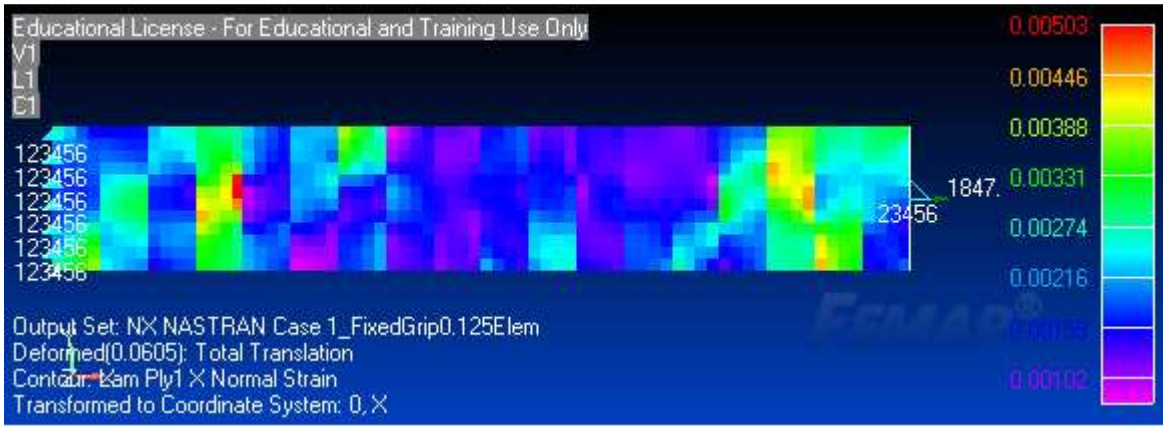

Figure 38: 3.18 mm (0.125 inch) Elements

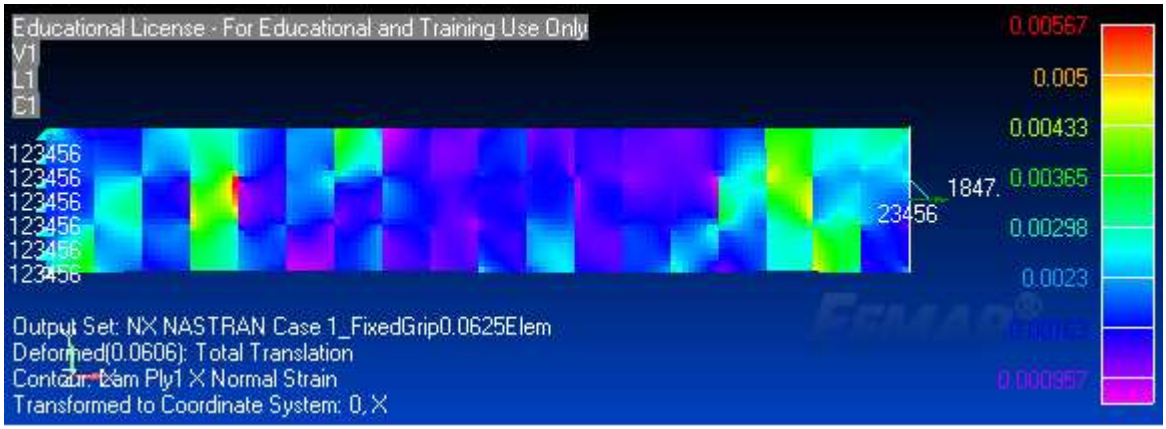

Figure 39: 1.59 mm (0.0625 inch) Elements

4.3. Results and RLVE Sizing

4.3.1. Experimental Results

Modulus Variation

The DIC images from each test were analyzed. Figures 40 and 41 show the strain field displacements for two sample specimens of each thickness.

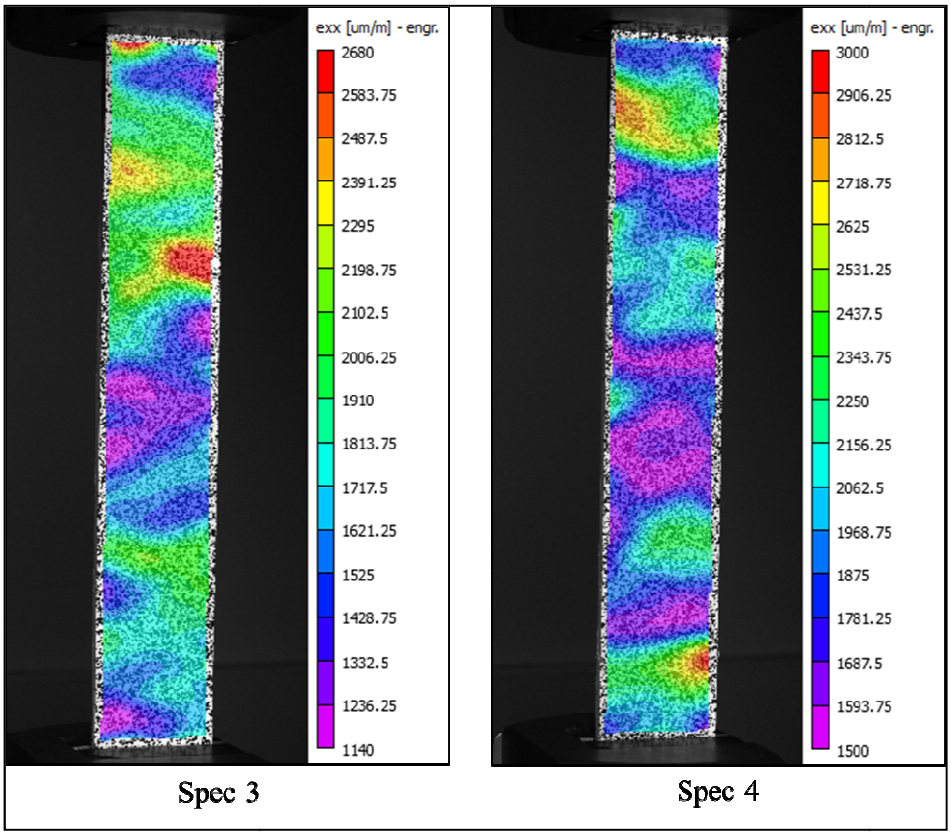

Figure 40: Modulus Variation - Thick

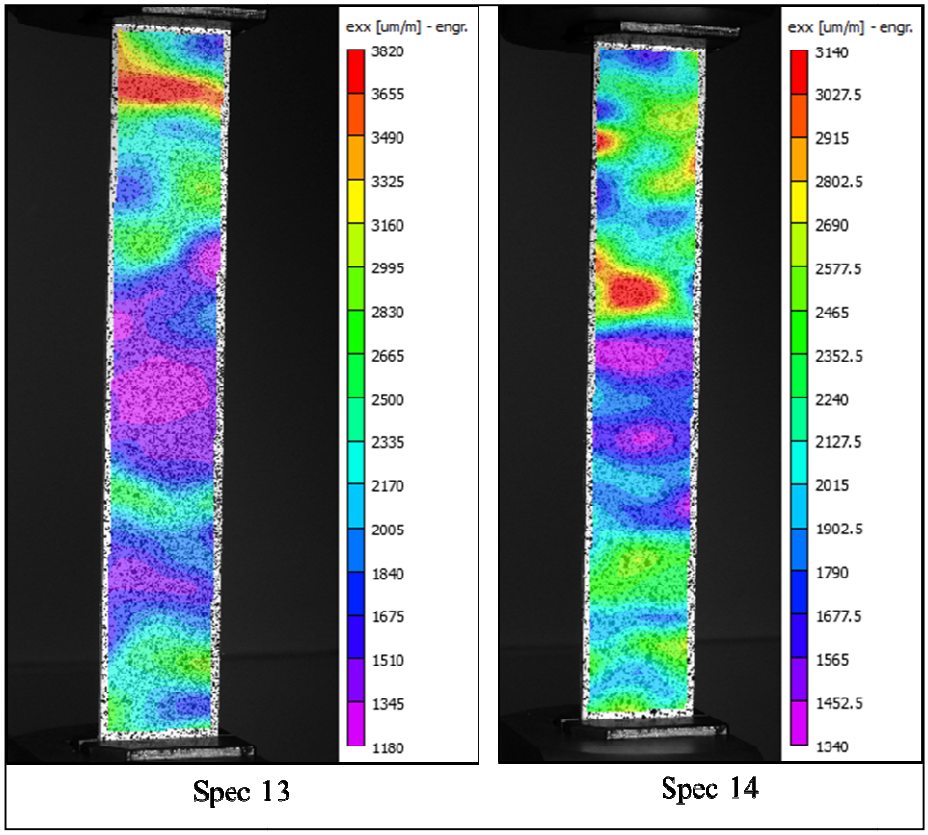

Figure 41: Modulus Variation - Thin

For each test, the effective modulus over 4 gauge region sizes was evaluated, as well as the maximum magnitude of out-of-plane displacements. The smallest gauge region was 25.4 mm x 6.35 mm (1 inch x 0.25 inch), corresponding to a one inch long strain gauge. The other gauge regions correspond to ¼, ½ and the whole surface. The ¼ and ½ surface regions are 114 mm x 19.1 mm (4.5 inch x 0.75 inch), 114 mm x 38.2 mm (4.5 inch x 1.5 inch). Over these regions the average strain on the surface is measured using DIC. The last region is an extensometer measurement using the DIC. The distance between measurement points for the extensometer was 228 mm (9 inch). With the exception of the whole surface gauge region, the strain measurements were taken at least 25 mm (1 inch) away from either grip, to ensure that boundary effects did not affect results. The average

strain over the smallest region was taken from two regions on each specimen. Since the region was so small, two independent measurements were able to be taken, doubling the sample size. Figure 42 shows the gauge regions over which average strain was measured. The entire surface gauge region was evaluated using an extensometer tool in the DIC software package. Modulus was then calculated by dividing the nominal stress applied by the average measured strain. The moduli calculated over the four gauge regions for each specimen are listed in Table 13 and 14.

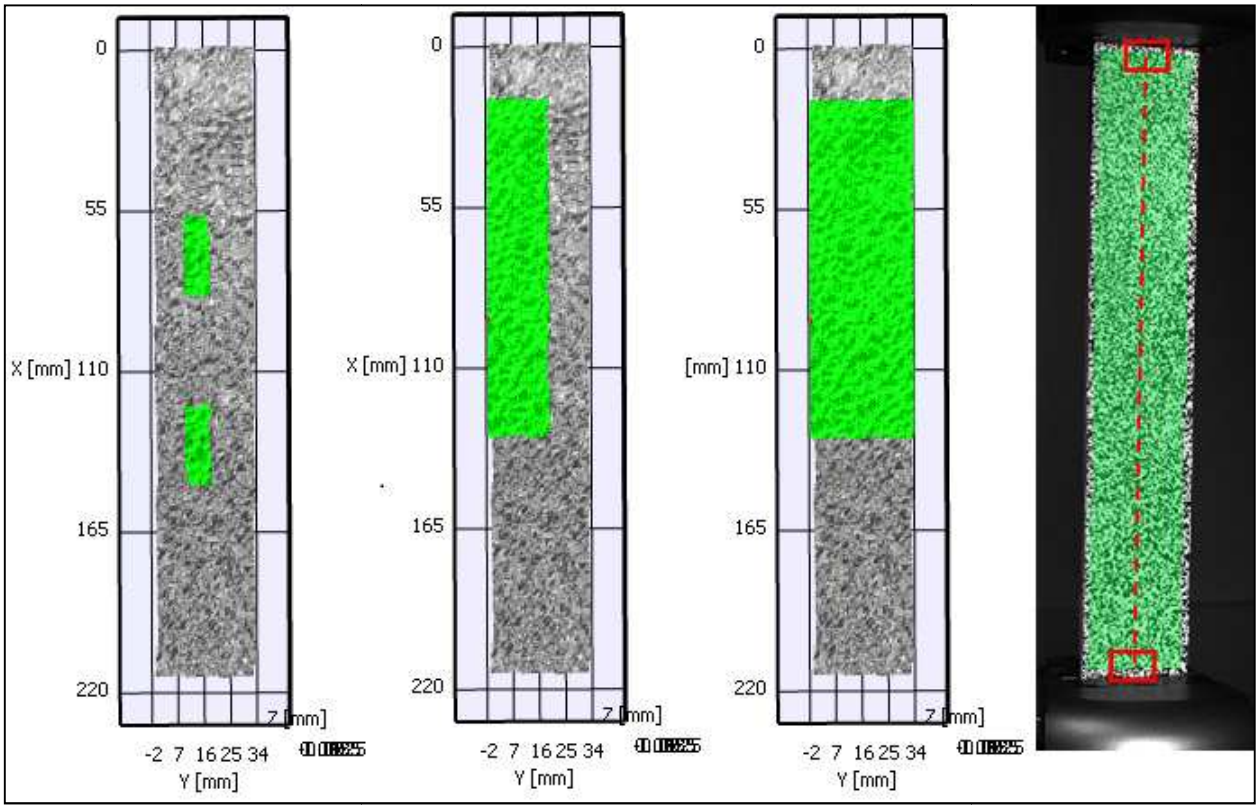

Figure 42: Gauge Regions

Table 14: Measured Modulus - Thick

	G1 GPa (Msi)	G2 GPa (Msi)	1/4 Surf GPa (Msi)	1/2 Surf GPa (Msi)	Ext GPa (Msi)
Spec 1 S1	54.2 (7.87)	55.5 (8.06)	52.1 (7.56)	52.1 (7.55)	48.8 (7.09)
Spec 1 S2	49.4 (7.16)	42.0 (6.09)	49.2 (7.13)	49.0 (7.11)	49.6 (7.20)
Spec 2	52.5 (7.62)	44.7 (6.49)	49.2 (7.15)	48.9 (7.10)	47.8 (6.94)
Spec 3	52.9 (7.68)	46.0 (6.68)	49.0 (7.11)	48.9 (7.10)	50.1 (7.28)
Spec 4	46.3 (6.72)	42.4 (6.15)	47.0 (6.81)	47.6 (6.91)	44.4 (6.44)
Spec 5	45.4 (6.58)	44.7 (6.48)	42.6 (6.18)	42.7 (6.20)	42.0 (6.09)
Spec 6	44.3 (6.42)	50.5 (7.33)	42.8 (6.21)	43.6 (6.32)	44.6 (6.47)
Spec 7	35.4 (5.14)	55.9 (8.11)	42.7 (6.20)	42.5 (6.17)	43.8 (6.36)
Spec 8	40.6 (5.89)	51.3 (7.45)	45.5 (6.60)	46.9 (6.81)	45.5 (6.61)
Spec 9	45.8 (6.65)	46.0 (6.67)	49.0 (7.11)	48.2 (6.99)	46.0 (6.67)

Min	35.4 (5.14)	42.6 (6.18)	42.5 (6.17)	43.8 (6.09)
Avg	47.3 (6.86)	46.9 (6.81)	47.0 (6.83)	46.3 (6.71)
Max	55.9 (8.11)	52.1 (7.56)	52.1 (7.55)	50.1 (7.28)

St Dev	5.1 (0.74)	3.3 (0.49)	3.1 (0.46)	2.7 (0.39)

Table 15: Measured Modulus (Msi) - Thin

	G1 GPa (Msi)	G2 GPa (Msi)	1/4 Surf GPa (Msi)	1/2 Surf GPa (Msi)	Ext GPa (Msi)
Spec 11 S1	40.8 (5.92)	44.5 (6.46)	42.6 (6.19)	42.5 (6.16)	42.5 (6.16)
Spec 11 S2	50.1 (7.27)	44.2 (6.41)	44.3 (6.43)	43.7 (6.34)	43.0 (6.24)
Spec 12	48.4 (7.02)	47.4 (6.87)	46.4 (6.74)	46.0 (6.67)	44.9 (6.52)
Spec 13	43.6 (6.32)	52.0 (7.55)	49.5 (7.18)	50.4 (7.31)	42.7 (6.19)
Spec 14	48.2 (7.00)	34.7 (5.03)	45.7 (6.63)	45.3 (6.57)	42.2 (6.12)
Spec 15	58.4 (8.47)	45.1 (6.55)	43.6 (6.32)	43.4 (6.30)	44.3 (6.42)
Spec 17	47.9 (6.95)	47.9 (6.94)	45.5 (6.60)	46.1 (6.69)	43.3 (6.29)
Spec 18	31.5 (4.57)	51.0 (7.40)	39.0 (5.66)	39.6 (5.75)	39.9 (5.79)
Spec 19	45.5 (6.60)	56.7 (8.23)	48.1 (6.98)	48.1 (6.97)	47.6 (6.90)
Spec 20	40.1 (5.81)	60.1 (8.72)	39.6 (5.74)	39.4 (5.72)	42.5 (6.17)

Min	31.5 (4.57)	39.0 (5.66)	39.4 (5.72)	39.9 (5.79)
Avg	46.9 (6.81)	44.4 (6.45)	44.4 (6.45)	43.3 (6.28)
Max	60.1 (8.72)	49.5 (7.18)	50.4 (7.31)	47.6 (6.90)

St Dev	7.1 (1.04)	3.4 (0.49)	3.5 (0.50)	2.0 (0.29)

Out-of-Plane Displacement Measurement

When testing began it was immediately apparent that measurement of the out-of-plane displacements due to membrane bending coupling was going to be difficult. The plates the specimens were cut from were not measured for flatness before being cut up and after being cut the specimens were not flat. When post-processing started, it was noticed that the specimens were curved at zero load, and then as the load increased they flattened out, then continued on past flat to exhibit out-of-plane displacements in the opposite direction of their initial shape. It was decided that during the portion of the test where the specimen was being pulled flat, the out-of-plane displacements were not due to strictly membrane-bending coupling, but rather simply being pulled flat. The displacements past flat however were interpreted to be due strictly to membrane-bending coupling. It was decided that the specimen would be considered flat when the standard deviation of the out-of-plane position was at a minimum. Figures 43 through 46 show specimen 3, 4, 13, and 14 at three points during the test, looking at the specimen edge on. For reference in the images shown, the load is being applied to the right in the image, and the DIC cameras were observing the top surface of the specimen, looking from the top of the page, towards the bottom. In this image the out-of-plane dimension, up and down as seen in the image, is greatly scaled, so that detail can be seen. All three images are shown with the same scale in the out-of-plane dimension. The three images are the start of the test, the point at which the specimen is considered flat by standard deviation calculation, and the end of the test. It can be seen that most of the out-of-plane displacement is the specimen flattening out. It can also be seen that initial un-flatness of the specimen is not necessarily predictive of the amount of post-flat displacement.

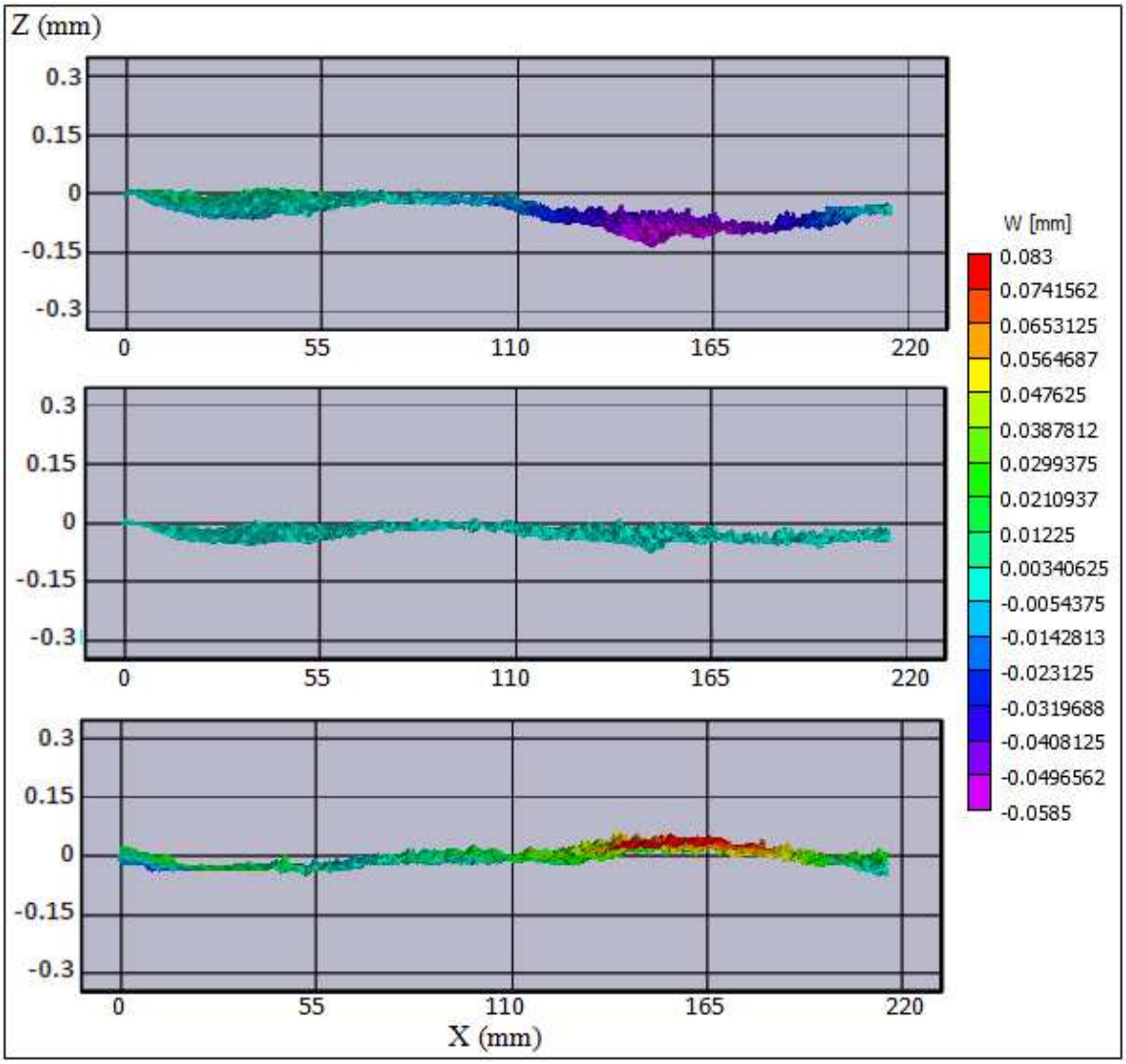

Figure 43: Spec 3

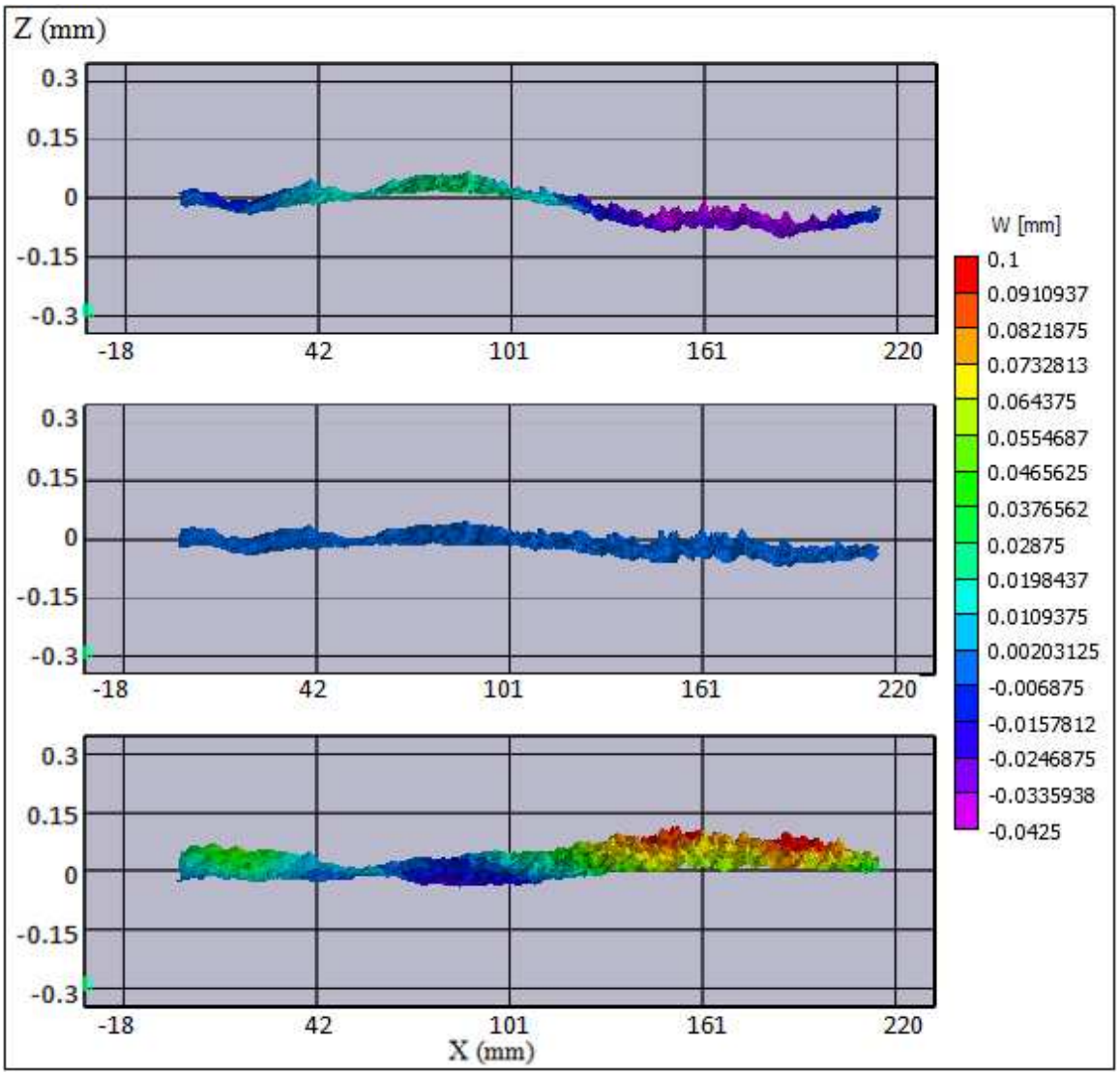

Figure 44: Spec 4

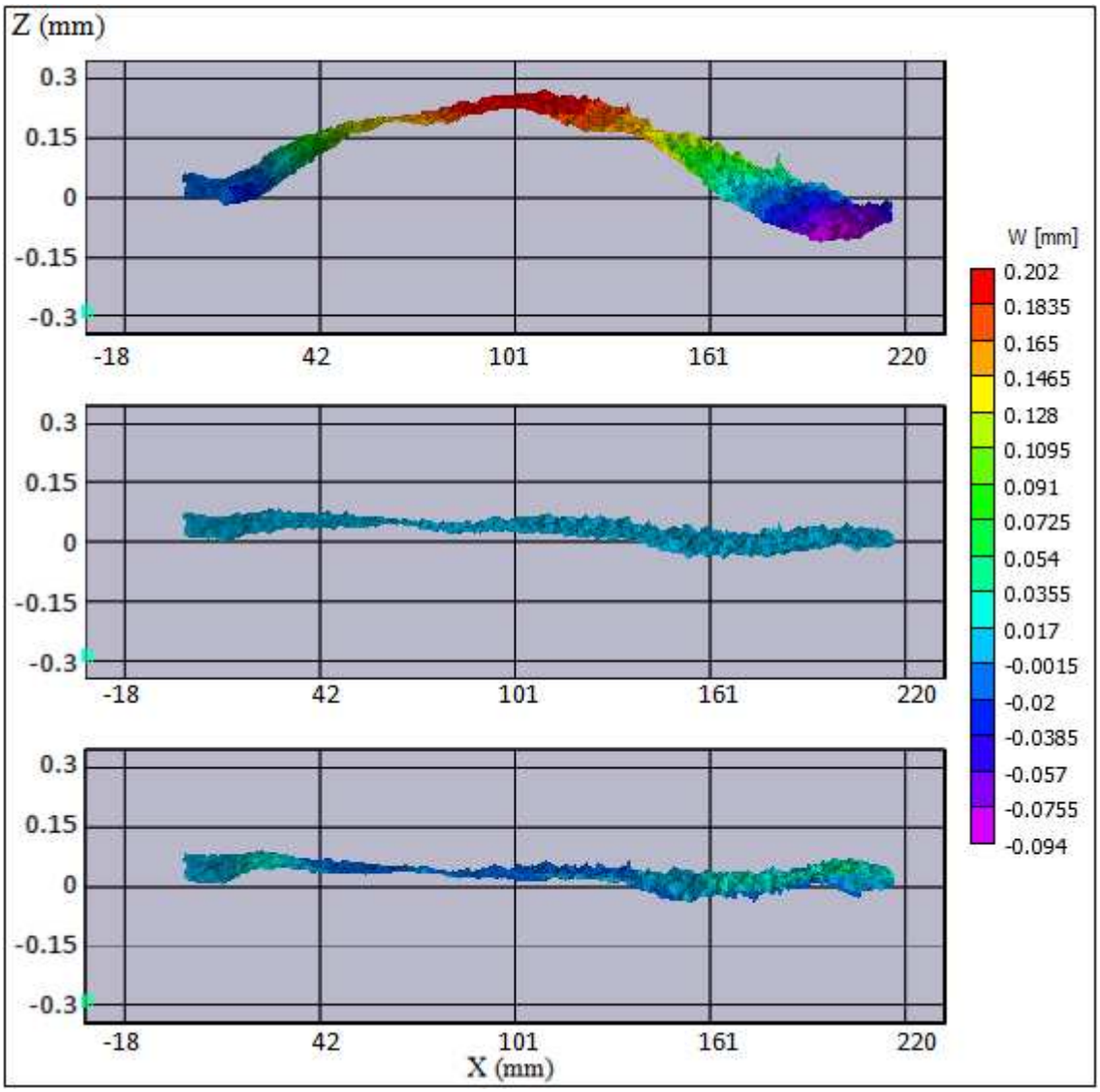

Figure 45: Spec 13

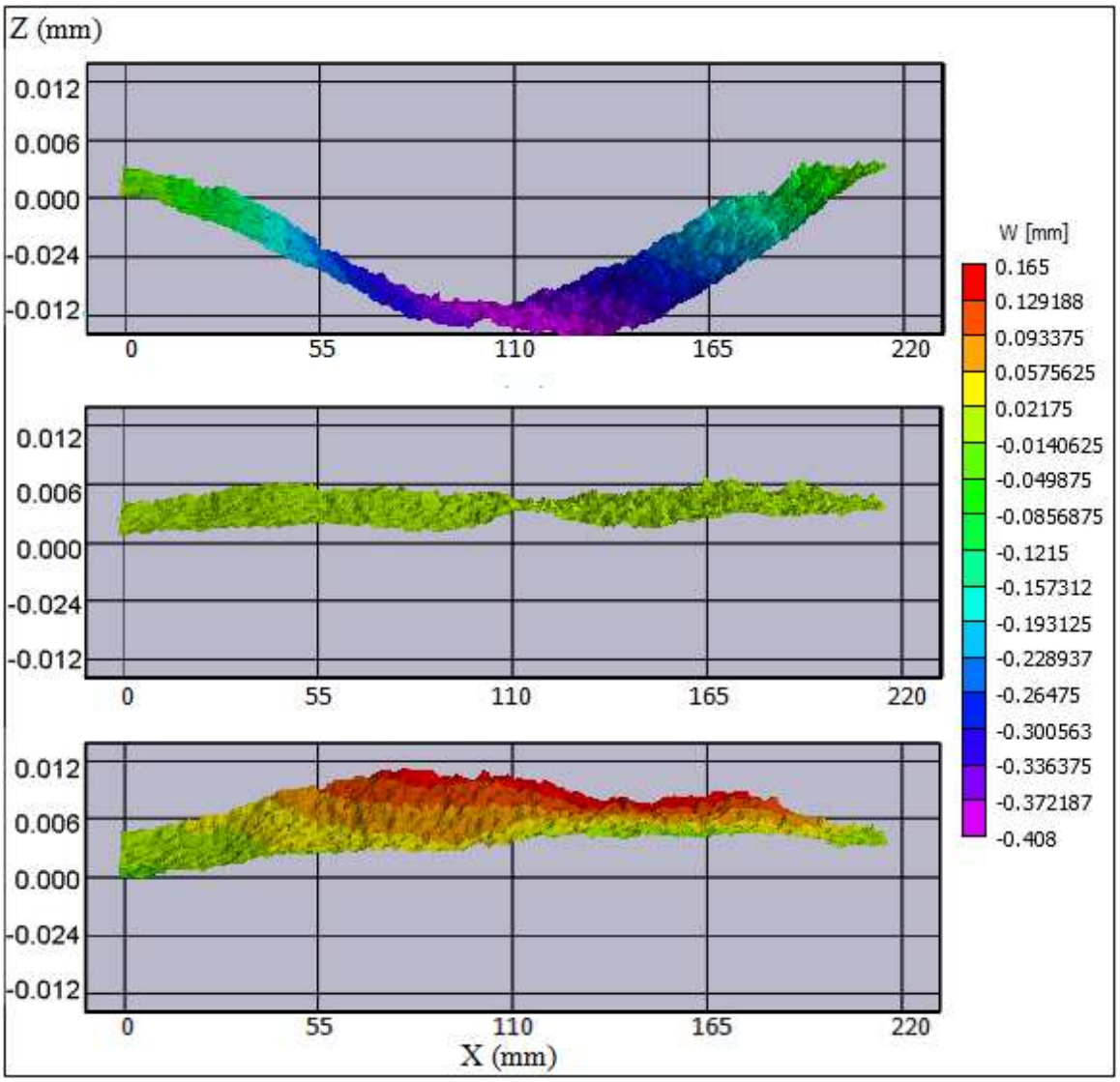

Figure 46: Spec 14

Once the reference for every test was found, the amount of membrane coupling was quantified with what will be called the coupling factor, which is the out-of-plane displacement per stress applied. This factor is calculated from the flat reference to 0.002 inches of out-of-plane displacement because as shown in Figure 47 as the out-of-plane displacement increases, the rate decreases. This is believed to be due to the fact that the farther from flat the specimen becomes, the more the in plane load fights the coupling, by

trying to pull the specimen flat. The limit was chosen because over all the specimens it seemed to be the best middle ground between remaining in the linear region and getting a large enough sample so that the effect of noise in the measurement was minimized. As shown by the linear fit in Figure 47, specimen 14 had a coupling factor of 4.68 mm/GPa (1.24 in/Msi).

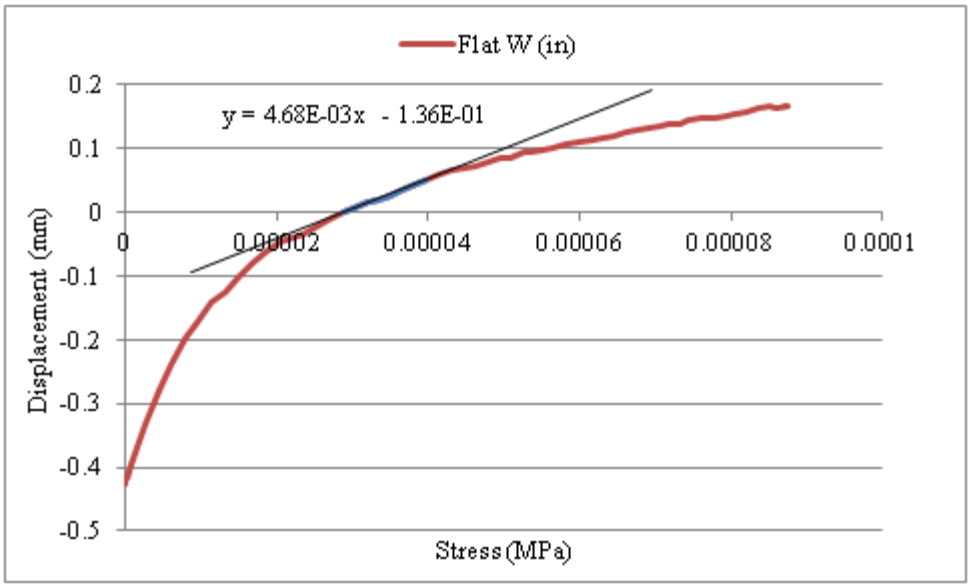

Figure 47: Spec 14 Coupling Factor

Unfortunately the coupling factors were not able to be consistently measured across multiple rounds of testing. Figure 48 shows a plot of the coupling factors for the same set of specimens measured on two different days. It can be seen that seemingly identical tests of a single specimen can yield coupling factors different by as much as a factor of three. The error in these measurements is due to several factors, the greatest of which is believed to be the initial waviness of the specimens. This made it difficult to determine what was due to coupling effects, and what was due to flattening of the specimen. Another complicating factor is the small scale of the displacements. The accuracy of the

DIC system at such small displacements made the measurements difficult. During several tests, the DIC calculated that the specimens exhibited out-of-plane displacements at the grips up to half as large as the greatest displacements away from the grip. These displacements were very small, on the order of a thousandth of an inch, but when considering that the coupling factor was determined over only two thousands of an inch, they become non-negligible. For this reason it was decided that RLVE size would have to be chosen by modulus variation alone.

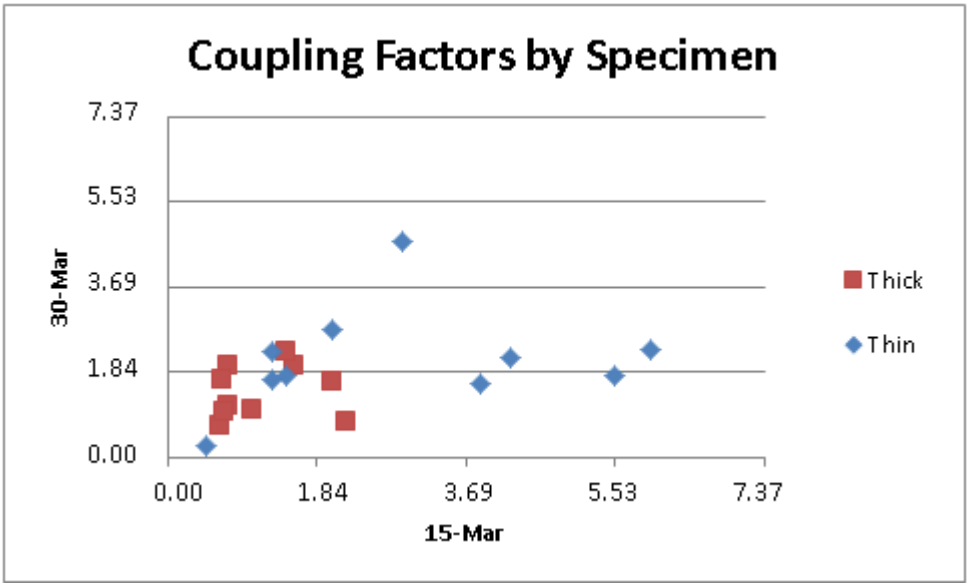

Figure 48: Coupling Factor Scatter (mm/GPa)

4.3.2. Modeling Predictions

Modulus Variation

Five thousand analysis runs were run for each of the three RLVE sizes chosen. For every run, average strain over four gauge regions was recorded. By dividing the nominal stress applied, a value for effective modulus over each gauge region was calculated. The four

gauge regions correspond to the same four gauge regions that were analyzed during testing. Figure 49 shows example contour plots of predicted strain variation on the surface for the three RLVE sizes. All three models are the thinner of the two thicknesses.

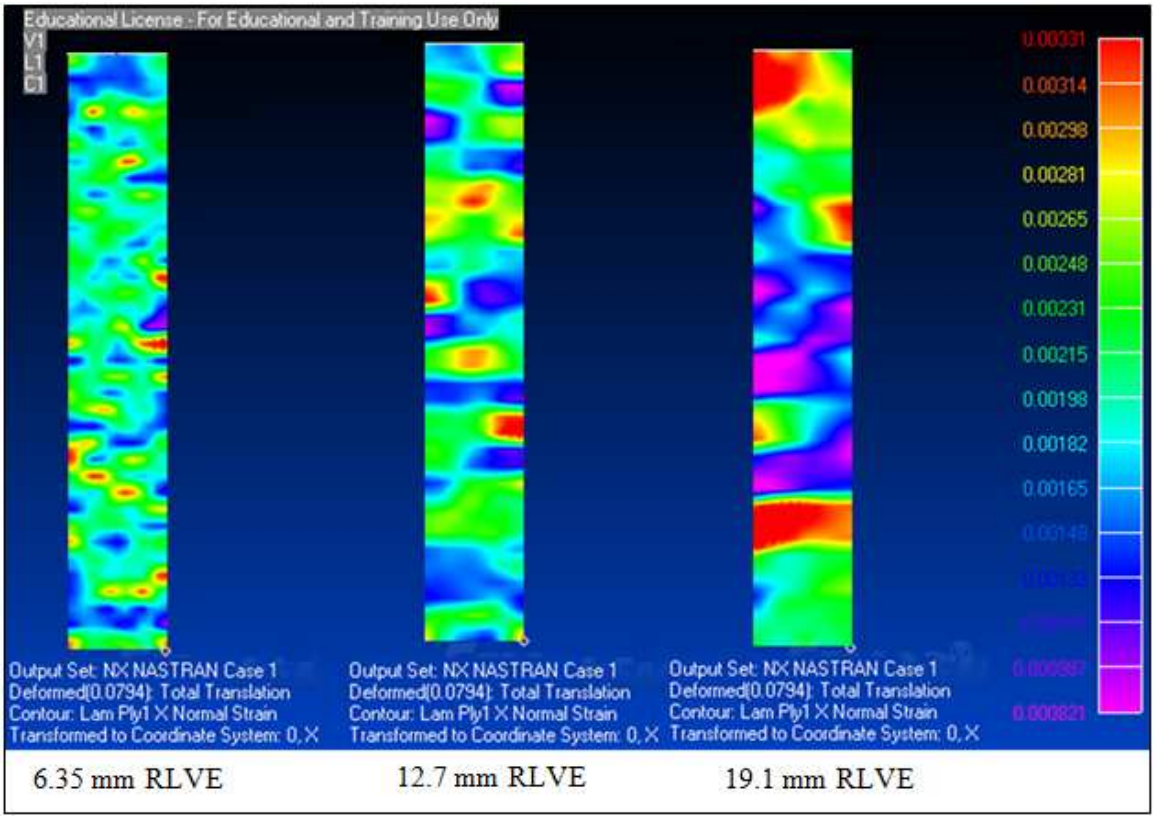

Figure 49: Axial Strain Contours

Tables 15 and 16 show the average modulus predicted over the four gauge regions for all 5000 runs for both thicknesses, as well as the error of the modulus measured over the largest region compared to the modulus obtained using the largest gauge region using DIC.

Table 16: Thick Spec Modulus Prediction

Thick	6.35 mm RLVE		12.7 mm RLVE		19.1 mm RLVE	
Gauge Area cm^2 (in^2)	Avg GPa (Msi)	St Dev GPa (Msi)	Avg GPa (Msi)	St Dev GPa (Msi)	Avg GPa (Msi)	St Dev GPa (Msi)
1.61 (0.25)	44.9 (6.52)	3.38 (0.49)	45.1 (6.55)	5.36 (0.78)	45.5 (6.60)	7.58 (1.10)
21.8 (3.38)	44.7 (6.49)	1.17 (0.17)	44.6 (6.47)	2.19 (0.32)	44.5 (6.45)	3.10 (0.45)
43.5 (6.75)	44.7 (6.49)	0.96 (0.14)	44.6 (6.47)	2.03 (0.30)	44.4 (6.44)	2.83 (0.41)
87.1 (13.5)	45.0 (6.53)	0.48 (0.07)	44.8 (6.50)	1.03 (0.15)	44.6 (6.47)	1.59 (0.23)
Error[(1)]	-2.76%		-3.18%		-3.64%	

Table 17: Thin Spec Modulus Prediction

Thin	6.35 mm RLVE		12.7 mm RLVE		19.1 mm RLVE	
Gauge Area cm^2 (in^2)	Avg GPa (Msi)	St Dev GPa (Msi)	Avg GPa (Msi)	St Dev GPa (Msi)	Avg GPa (Msi)	St Dev GPa (Msi)
1.61 (0.25)	44.1 (6.40)	4.15 (0.60)	44.6 (6.47)	7.33 (1.06)	45.0 (6.53)	9.79 (1.42)
21.8 (3.38)	43.9 (6.37)	1.43 (0.21)	43.5 (6.31)	2.81 (0.41)	43.3 (6.28)	3.92 (0.57)
43.5 (6.75)	43.8 (6.36)	1.31 (0.19)	43.5 (6.31)	2.59 (0.38)	43.2 (6.27)	3.65 (0.53)
87.1 (13.5)	44.1 (6.40)	0.74 (0.11)	43.7 (6.34)	1.39 (0.20)	43.4 (6.29)	1.98 (0.29)
Error[(1)]	1.91%		1.00%		0.21%	

[(1)] Error is comparison between experiment and prediction of modulus over largest gauge region

Coupling Prediction

Along with predicting local modulus variation, the stochastic model predicts out-of-plane displacement when an in plane load is applied. Figure 50 shows an example analysis run, displaying the out-of-plane displacements for the 19.1 mm RLVE model, shown in Figure 49, scaled by a factor of 10.

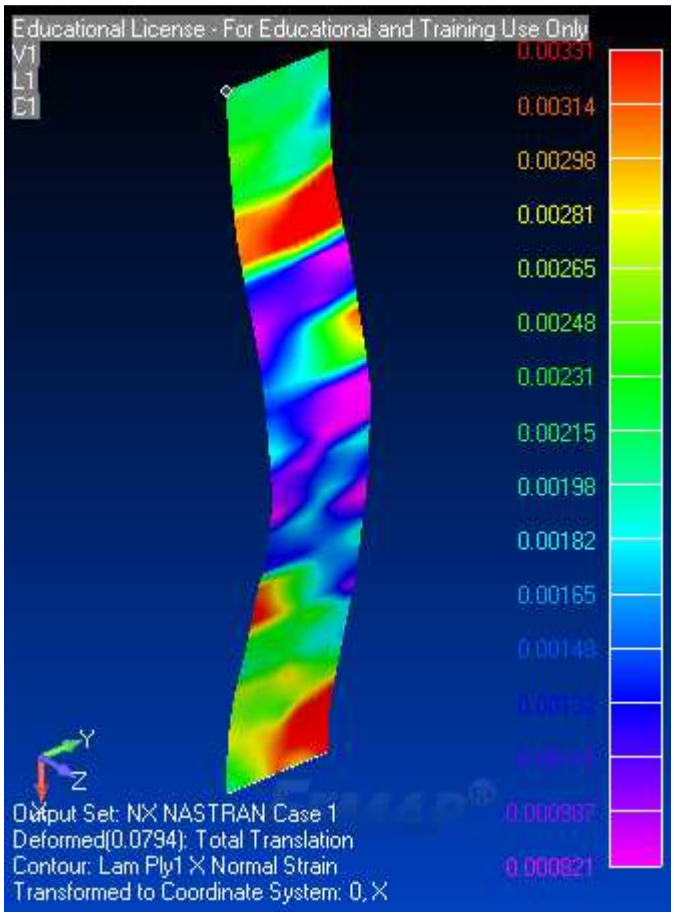

Figure 50: Predicted Coupling (10X)

For each analysis run, along with recording the average strains over the various gauge regions, the maximum and minimum out-of-plane displacement was also recorded. The greatest magnitude of out-of-plane displacement for each run was divided by the applied

nominal stress, to obtain a coupling factor comparable to that which was calculated in the previous section. Table 18 lists the average coupling factor for both thicknesses for each of the three RLVE sizes. It also lists the standard deviation of the coupling factor over all 5000 runs. Since it was determined that the coupling factors could not be reliably measured, the values here are presented to show that predicted values are of the same order of magnitude as those measured.

Table 18: Coupling Factors

	Thick			Thin		
	6.35 mm RLVE	12.7 mm RLVE	19.1 mm RLVE	6.35 mm RLVE	12.7 mm RLVE	19.1 mm RLVE
Avg mm/GPa (in/Msi)	1.29 (0.35)	2.30 (0.62)	3.74 (1.01)	2.55 (0.69)	5.05 (1.37)	7.67 (2.08)
St Dev Mm/GPa (in/Msi)	0.50 (0.13)	0.96 (0.26)	1.52 (0.41)	1.04 (0.28)	2.12 (0.58)	3.25 (0.88)

4.3.3. RLVE Sizing

Figure 51 shows the standard deviation of moduli over the various gauge regions for the three RLVE sizes (solid lines) as well as the experiments (dotted line) for the thick specimens. It can be seen that if the smallest gauge region is considered, the 12.7 mm (0.5 in) RLVE is suggested, however as the gauge regions considered grows, so does the suggested RLVE size. Figure 52 shows the same plot for the thin specimens

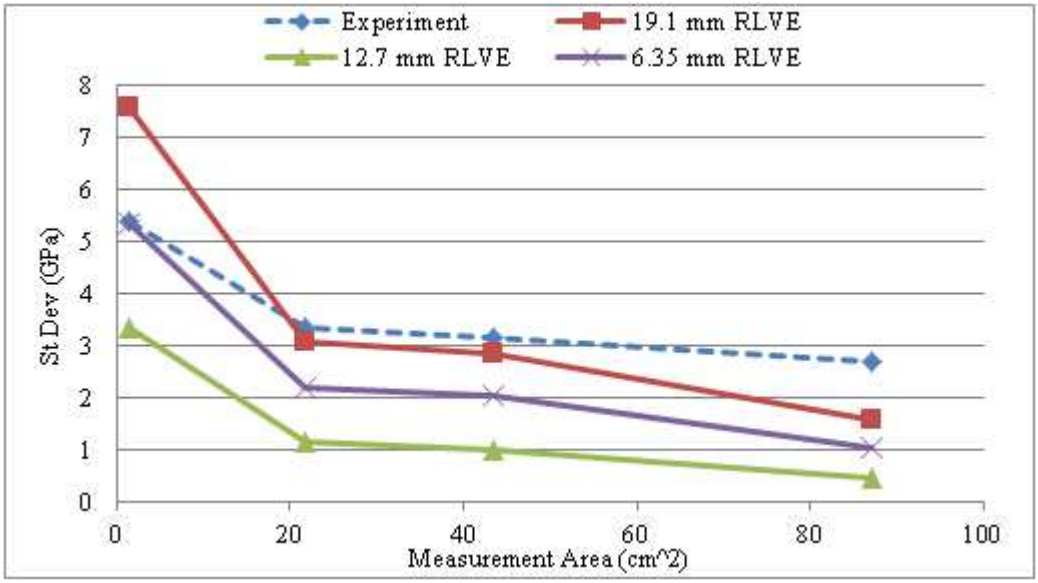

Figure 51: Modulus Variation - Thick

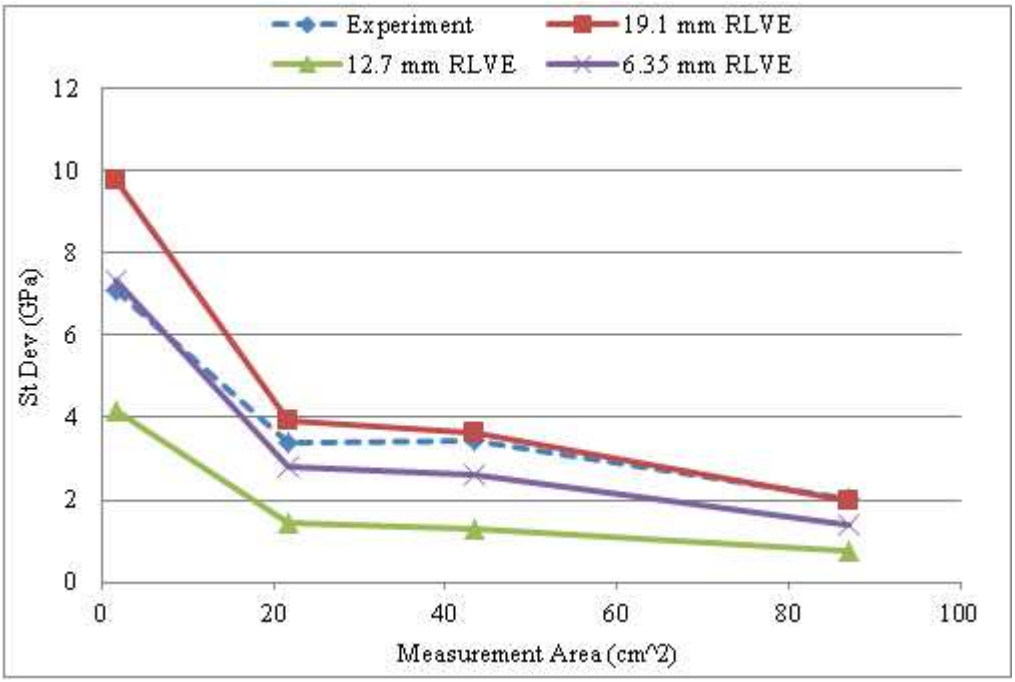

Figure 52: Modulus Variation - Thin

For both thicknesses the predicted variation among the largest gauge region is much lower than might be expected. This is due to the fact that the displacement based strain measurements, as opposed to the surface based ones, are nearly independent of surface variations due to bending of the specimen. This yields a more consistent measurement, and this behavior is also exhibited in the thin specimens. Table 19 shows the RLVE size suggested by interpolation for each gauge region for both thicknesses as well as the average size.

Table 19: Suggested RLVE Sizes

	Suggested RLVE Size mm (in)	
Gauge Area cm^2 (in^2)	Thick	Thin
1.61 (0.25)	12.7 (0.50)	13.0 (0.51)
21.8 (3.38)	20.8 (0.82)	16.3 (0.64)
43.5 (6.75)	21.6 (0.85)	18.0 (0.71)
87.1 (13.5)	32.3 (1.27)	19.6 (0.77)
Average	21.8 (0.86)	16.8 (0.66)

Taking the average of the two values, the suggested thickness independent RLVE size is be 19.3 mm x 19.3 mm (0.76 inches x 0.76 inches).

4.4. Stochastic Angle Modeling

The angle beams that were discussed in Section 3 were modeled again, using the RLVE size chosen by comparison to the tensile coupons. As was discussed, it was suspected that

the local stiffness variations combined with the membrane bending coupling were part of the cause of over predicting the buckling loads when isotropic properties were used.

4.4.1. Method

The RLVE method was applied to the angle beams much in the same way as to the flat specimens. The models were broken up into RLVEs of appropriate size then each RLVE was assigned a random stacking sequence. Figure 53 shows a model of a medium size angle broken up into RLVEs with mesh size shown.

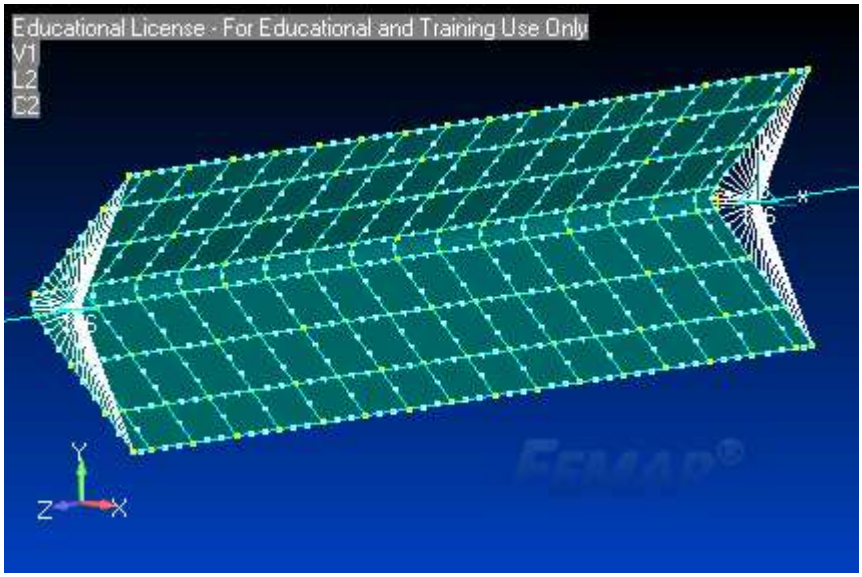

Figure 53: Medium Angle RLVE

The RLVE chips were assigned properties of the HexMC® precursor once again, but this time the properties in compression were used as is common for buckling analyses. The properties in compression were first tested in the same program used for the flat plate predictions. First, the properties were obtained by following the same procedure used to match resin content for the tensile properties. However the effective modulus in

compression predicted by this method was much lower than measured and reported by the Hexcel Allowables Report [16]. Because of this, the properties were adjusted to yield an average stiffness in compression equal to that which was reported by Hexcel and used for angle modeling in Section 3.4. For proprietary reasons, the properties cannot be listed here.

4.4.2. Displacement and Buckling Load Predictions

Each size of angle was modeled 10 times using the RLVE process. Each run took 13, 36, and 44 minutes for the small, medium and large angles respectively. Figures 54 through 56 show the comparison between the B-range predictions and the maximum and minimum for buckling predictions from the 10 RLVE runs for each angle size.

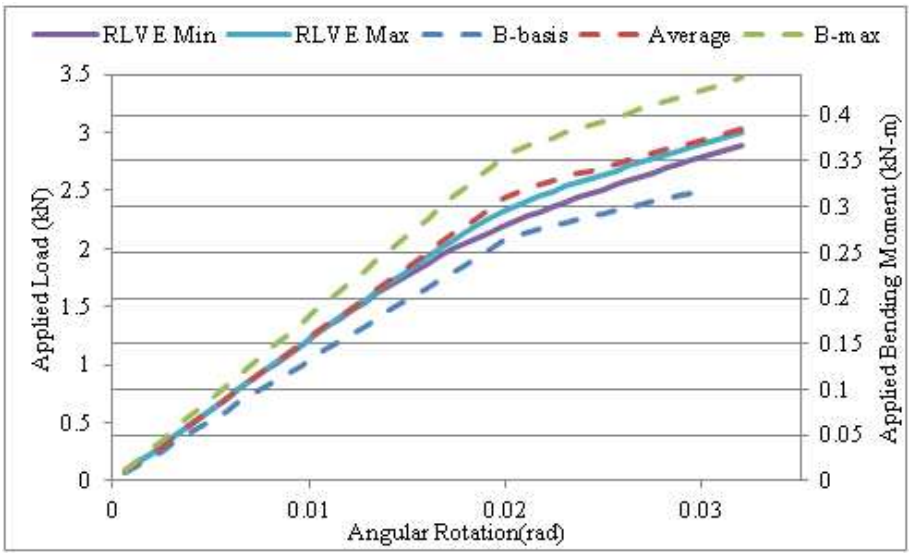

Figure 54: Small RLVE Comparison

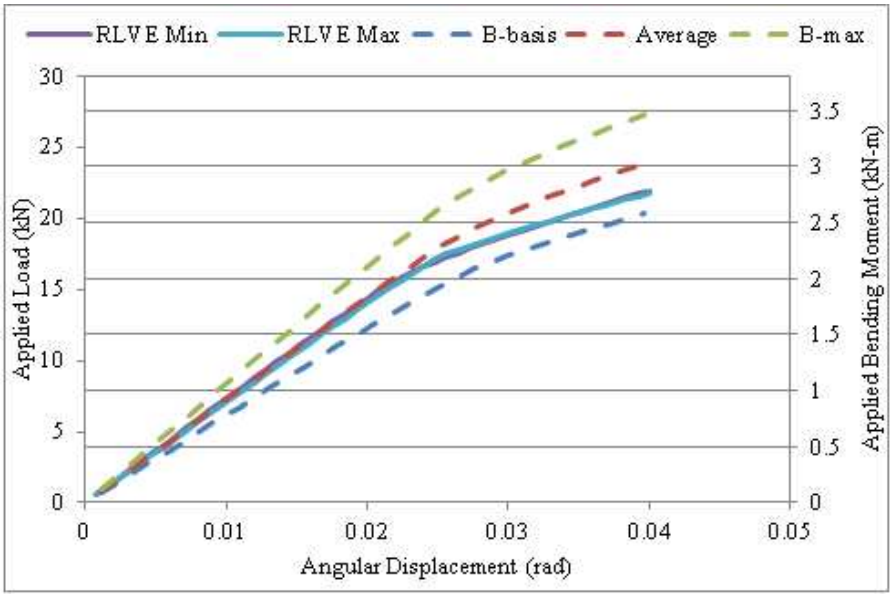

Figure 55: Medium RLVE Comparison

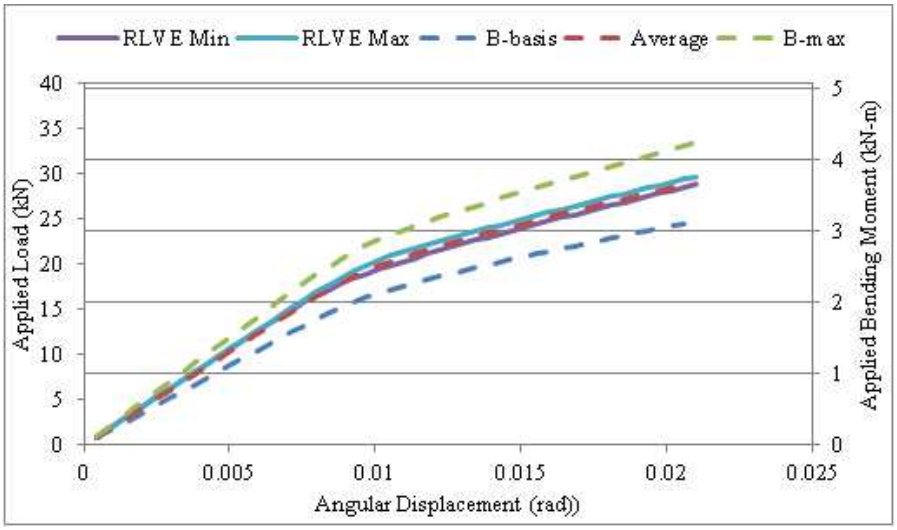

Figure 56: Large RLVE Comparison

It can be seen that for all angle sizes the variation in pre-buckling displacements was not predicted. For the small angle there was a substantial range in predicted buckling loads.

For the medium and large angle the range in predicted buckling load was much lower. This suggests that as part size and/or thickness increases, the effects of membrane coupling decrease. This suggests that there might be a minimum thickness under which membrane coupling effects become increasingly important to consider. Figures 57 and 58 show the experimental buckling loads of the tested angles along with the 10 predicted buckling loads for the small and large angles respectively. Also displayed are the low and high buckling loads predicted by the B-range moduli.

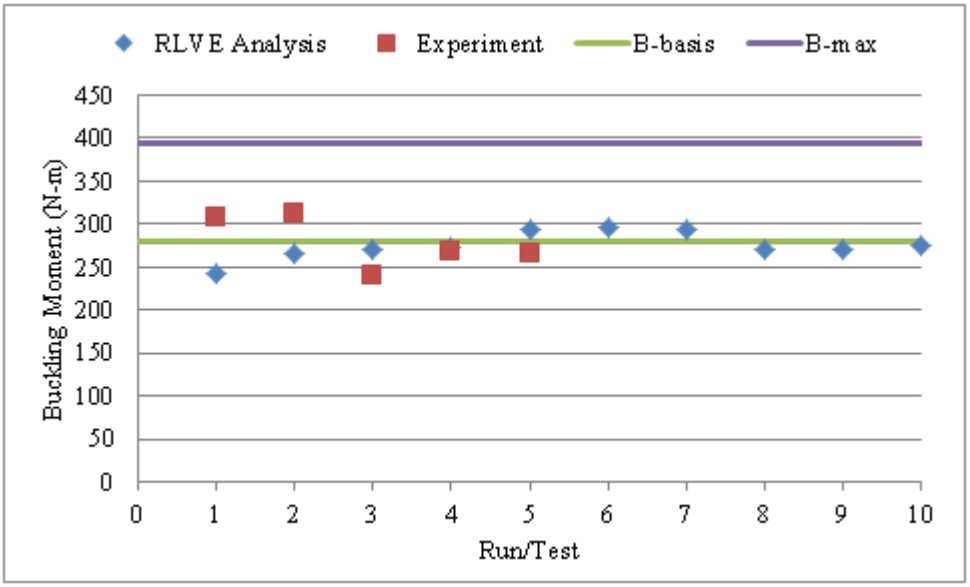

Figure 57: Small Buckling Loads Comparison

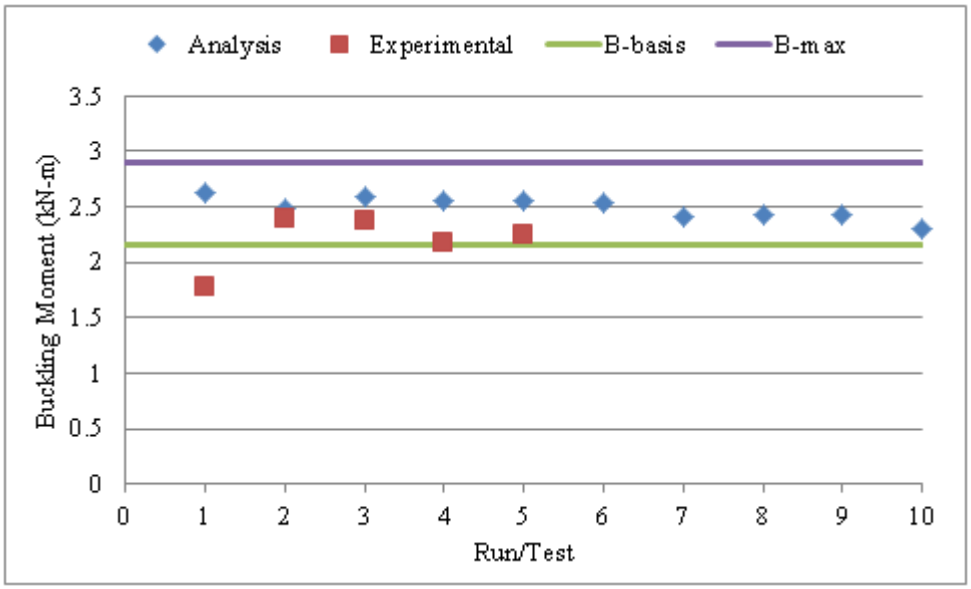

Figure 58: Large Buckling Loads Comparison

It can be seen for the small angles, despite the range in pre-buckling displacements being poorly predicted by the RLVE analysis, the range of buckling loads matched that seen experimentally well. The average buckling load was also very well predicted by the RLVE analysis. The same level of improvement was not seen for the large angles. The average buckling load predicted by the RLVE analysis was not substantially different that that predicted by the average isotropic modulus.

Figure 59: Medium Buckling Loads Comparison

Figure 59 shows the experimental failure load for the medium size angles tested compared with the buckling loads predicted by both the RLVE analysis as well as the B range moduli. It can be seen that the RLVE analysis predicted buckling at a lower level than the B range moduli. The RLVE analysis still predicted buckling right at or before the failure loads seen experimentally however, matching what was observed experimentally.

4.4.3. Discussion

The application of the RLVE method to the prediction of buckling of angle models failed to predict the variation in pre-buckled displacements. However, this approach did lead to improved buckling load predictions for the small angle size. The fact that essentially no variation in pre-bucking displacements was predicted suggests that the RLVE model does not capture the global modulus variation exhibited by HexMC® when applied to structures. It does predict reduced buckling loads when compared to the B-range

modulus. This suggests that the membrane coupling effects do play an important role in buckling loads for structures under a certain thickness.

5. HexMC® Brace Modeling

To extend the established practices to a more complex part, a bracket made from HexMC® was chosen. It has a four bolt pattern on one end, called the root, and a two bolt pattern on the other, called the clip. Figure 60 shows a 3-D solid model of the brace, where the root end can be seen on the left, and the clip end on the right.

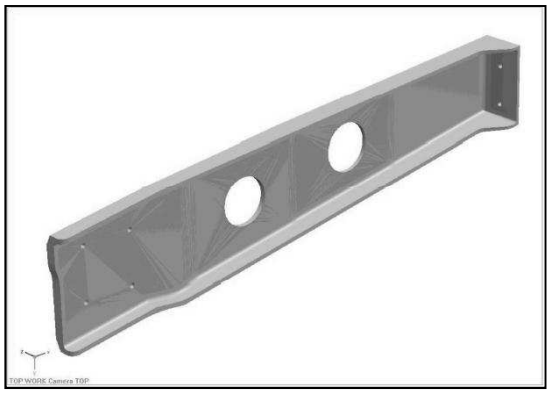

Figure 60: Brace

5.1. Guided Clip Test Setup

The braces were tested by The Hexcel Corporation at their Kent facility. The documentation of the testing is Hexcel proprietary, and as such, cannot be fully disclosed here [23]. During testing the root end was fully fastened to the test fixture using Hi-Lok® fasteners. The clip end was fastened to a plate, which was pulled on with a linear actuator. The clip end was prevented from rotating about the axis of the brace. Displacement of the clip end was measured using a Linear Variable Differential Transformer (LVDT).

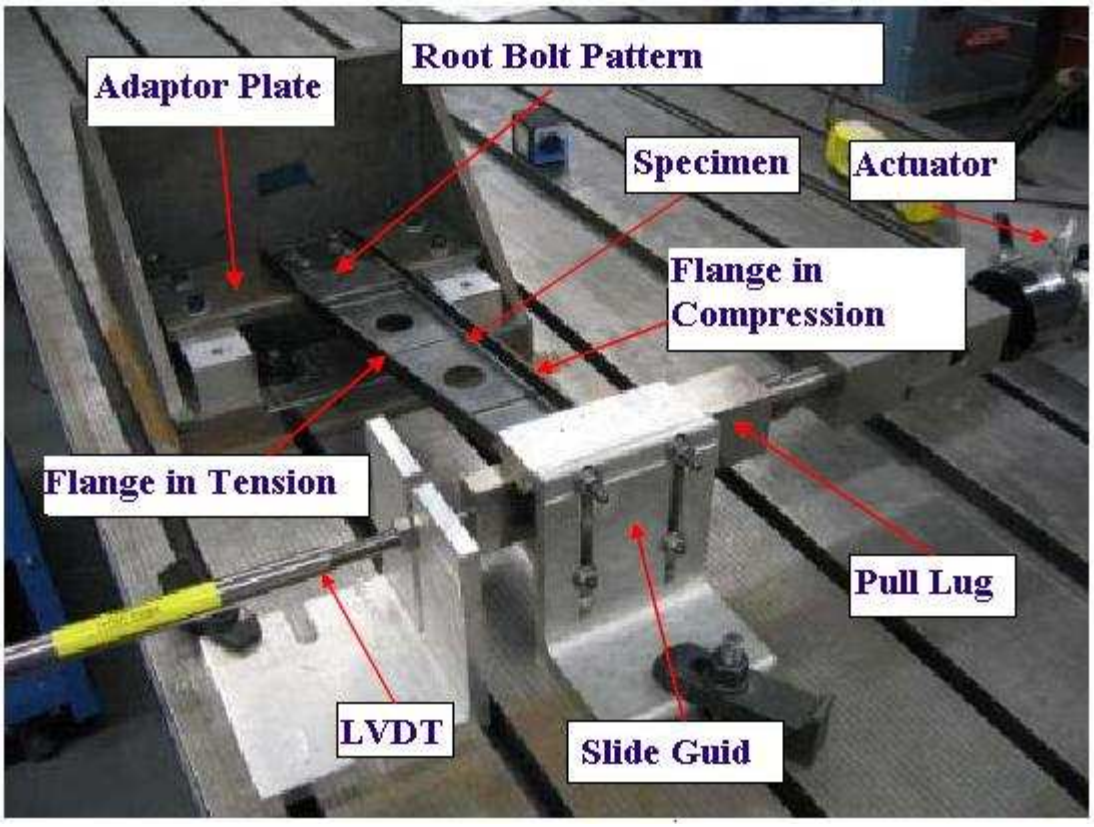

Figure 61: Guided Clip Test Setup [23]

In total, 25 specimens were tested to failure and considered in this study. The specimens were tested in two steps, first they were loaded to remove the slack from the connections, then unloaded. They were then loaded to failure.

5.2. Guided Clip Modeling

The brace was modeled using solid 10 noded tetrahedral elements. A mesh convergence study was preformed, to ensure predicted stresses were not mesh dependent. Satisfactory mesh convergence was achieved, with the exception of areas near the bolted regions, which will be further discussed in Section 5.3.2. The brace was modeled using the average modulus in tension, 6.62 Msi. Since only geometrically linear modeling was

done, modeling over the B range in moduli had no effect on failure predictions, and as such, was un-necessary. The root and clip connections were modeled as bolted connections, with the mounting plates assigned properties of 4340 steel, and the bolts with the properties of the titanium fasteners. Both the plates and bolts were modeled using solid elements, and 3-D contact was established between the bolts, brace, and mounting plates. The clip and root bolts were preloaded with 4360 N and 9090 N (960 lbf and 2000 lbf) each respectively, according to the tightening torque specified by the manufacturer and assuming a coefficient of friction of 0.2 [22]. A sensitivity study was done, and no significant effect on predicted displacements was found when pre-load was varied by ±10%. Figure 62 shows the model of the brace, mounting plates, and bolts before loads and boundary conditions were applied.

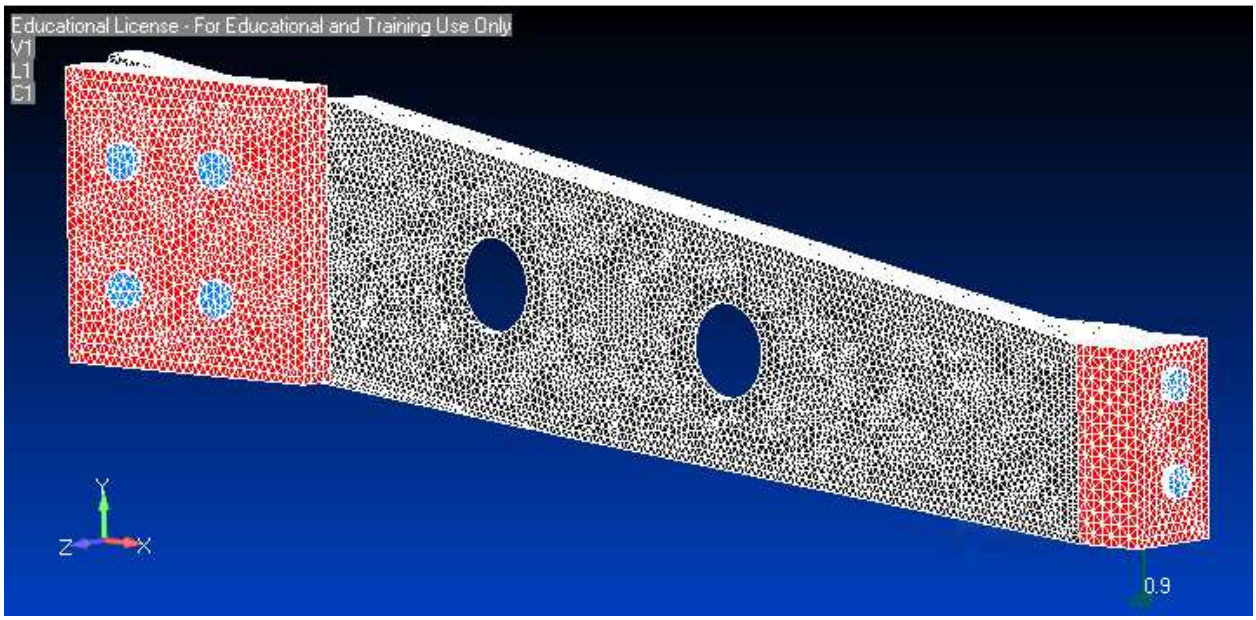

Figure 62: Brace Model

5.3. Guided Clip Experimental and Modeling Results

5.3.1. Testing Results

Figure 63 shows the load-displacement curves for seven of the tests to give an idea of what the curves looked like. All loads reported in Section 5.3 and 5.4 are normalized to the lowest measured failure load, to protect proprietary data. There is obviously some non-linear behavior exhibited as the load exceeds approximately 1.08 of the lowest failure load. The curves representing the highest of the failure loads are not shown in Figure 63 because they exhibited slipping, which made the curves difficult to compare. The braces tested failed in five distinct locations. The locations are depicted in **Error! Reference source not found.Error! Reference source not found.**. Table 20 lists the minimum and average failure load at each location.

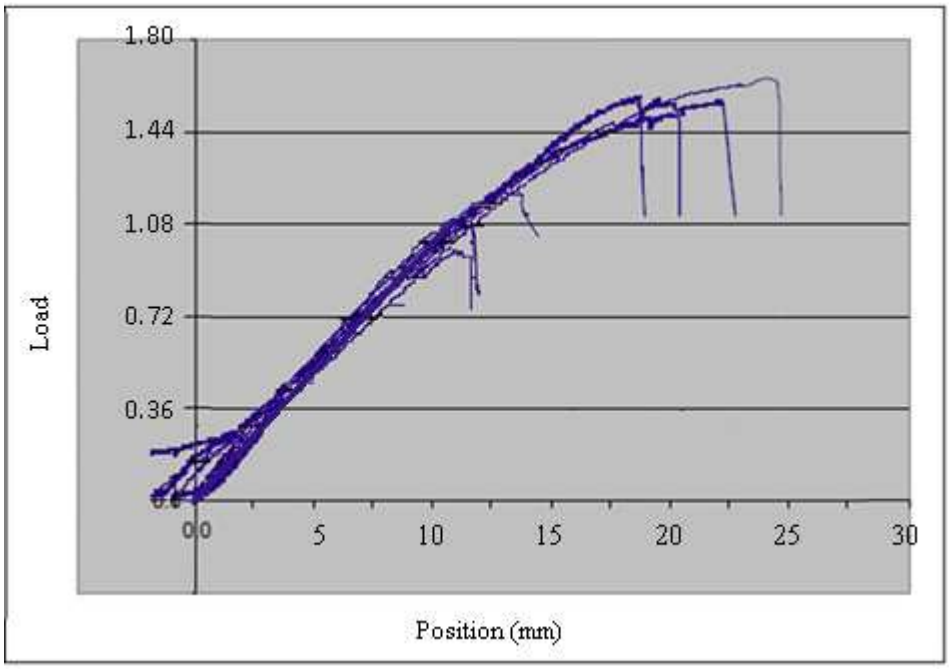

Figure 63: Brace Load - Displacement Profiles [23]

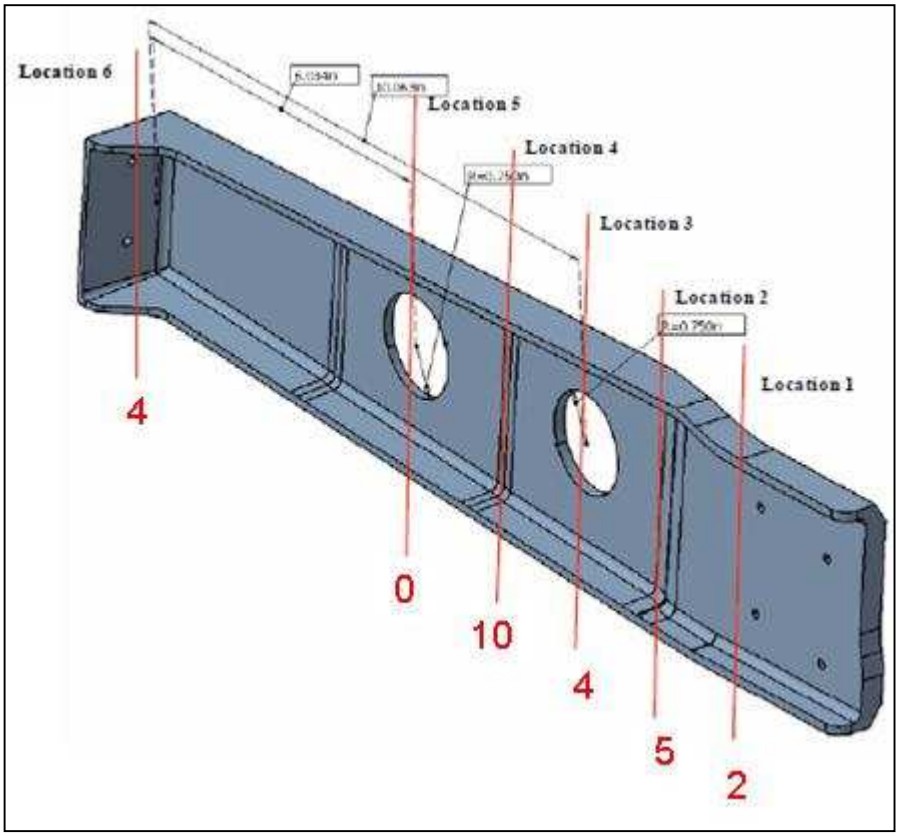

Figure 64: Failure Locations [23]

Table 20: Guided Brace Failure Loads by Location

Location	Normalized Minimum	Normalized Average
1	1.09	1.11
2	1.00	1.47
3	1.54	1.63
4	1.30	1.61
6	1.41	1.55

The failures seen at locations 2 through 4 were tensile failures of the web/flange of the brace. The failures seen at location 1 were through the bolt holes closest to the clip end. The failures seen at location 6 were characteristically peeling of the face of the clip end, off of the end of the brace.

5.3.2. Modeling Results

Figure 65 shows the predicted displacement compared to the measured. It can be seen that the model does not predict the non-linear behavior, since it is a linear model. When analyzed using Sol 601, geometrically non-linear behavior is not predicted until over three times the lowest failure load.

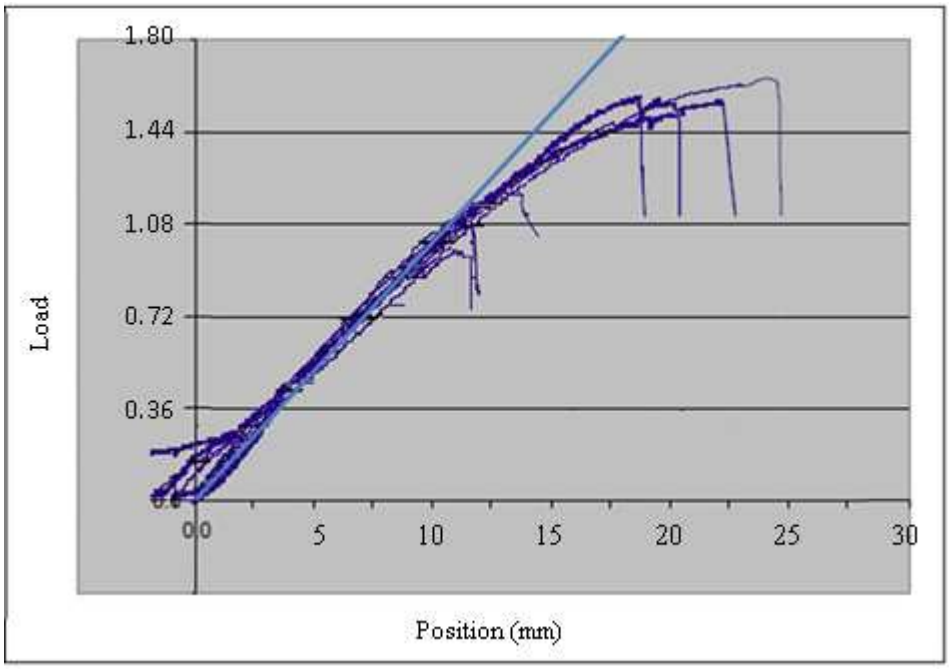

Figure 65: Brace Displacement Comparison

The predicted stress contours revealed six high stress regions on the brace. Figure 66 shows the Von Mises stress contour and outlines the regions over which the maximum stress was searched for in subsequent analysis.

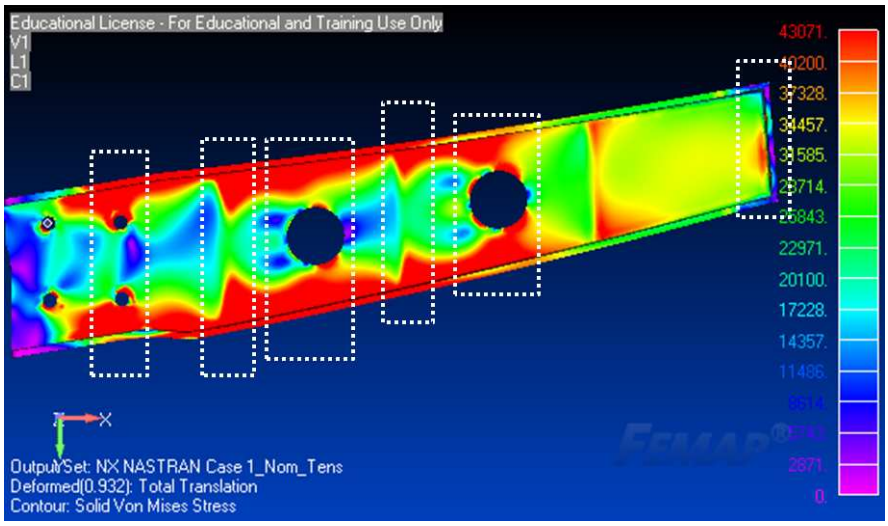

Figure 66: Brace Stress Contour

Figure 67 shows the interior region of the brace with the four highest stress locations depicted, with their respective stress, normalized to the largest one. It can be seen that the maximum stresses at all four locations are predicted to be within 17% of each other.

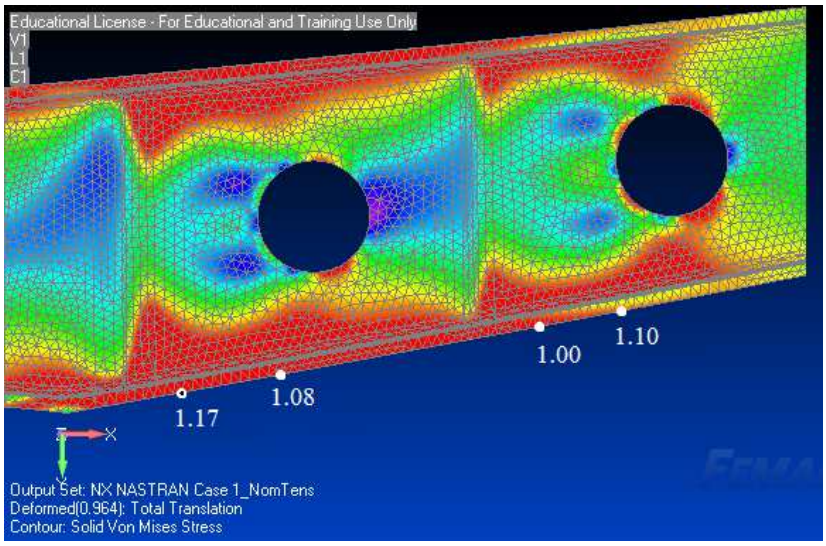

Figure 67: Normalized High Stress Regions

Failure was predicted at locations 2 through 4 by use of the max principal stress, Von Mises stress, and the Tsai-Wu failure criterion. Because the stress in those regions is roughly uniaxial, all three failure criteria yield the essentially the same prediction. The failure loads compared to the experimentally measured loads presented in Table 21 are based on the maximum principal stress compared to the B-basis or average strength in tension. With the exception of the low outlier in location two, the failure loads were well predicted by the use of average modulus and B-basis strength.

Table 21: Failure Load Comparison

	Test Min	Pred. Min	Error (%)	Test Avg.	Pred. Avg.	Error (%)
2	1.00	1.27	**26.8**	1.47	1.57	**7.3**
3	1.54	1.37	**-11.5**	1.63	1.70	**4.4**
4	1.30	1.50	**15.1**	1.61	1.86	**15.6**

Failure was predicted at the clip and root end using several criteria as well. In these regions, failure predictions were more difficult because of the stresses generated by the contact forces. In the root region, the stresses predicted in the bolt regions were extremely high. In addition to predictions based on FEA predicted stresses, failure at the bolt holes was also predicted using hand calculations of bearing stress compared to the stabilized bolted joint bearing strength of HexMC®.

Table 22: Root End Failure Loads

Exp. Failure	
Min	1.09
Max	1.13

Location 1		Pred. Failure
Von Mises	Failure	0.26
Hand Calc. Stab. Bearing	Yield	1.22
	Failure	1.70

The stresses predicted at the clip end are more complex than at the root. The bearing stresses are not high enough to predict bearing failures. Von Mises stresses predict the failure load the closest to what was measured experimentally, but predict a different failure mode than the peeling of the face that was seen.

5.4. Guided Clip Discussion

Away from the boundary conditions, the use of B-basis and average strengths compared to maximum or Von Mises stresses predict strength reasonably well, with the average error being less than 15%. When failure is to be predicted near bolted connections however, troubles arise. Many of these troubles arise from the treatment of the material as

an isotropic material, when in reality it is only approximately transversely isotropic. HexMC's out-of-plane modulus is much lower than if it were truly isotropic. This leads to over predicted out-of-plane stresses, and makes comparison to measured transverse tensile strengths impossible. It also eliminates the ability to attempt to use more traditional composite failure criteria, such as the 3-D version of the Tsai-Wu Criterion.

The benefit of modeling the brace using 10 noded tetrahedral elements is ease of meshing. Automatic meshing tools easily mesh the brace using tetrahedral elements. The downside is that only isotropic material properties can be used with this element. The use of transversely isotropic material properties could possibly greatly improve predictions, especially in the region of the clip end. Using isotropic material properties, transverse shear and normal stresses were predicted, both of which could cause the peeling failure seen experimentally. However the predicted transverse and normal stresses in these regions are not reliably predicted, because the out-of-plane properties used are not representative of HexMC®.

In the root region, failure was best predicted using hand calculations of bearing stress and stabilized bearing strength. Predictions in this region may also benefit from the use of in-plane isotropic properties, bringing FEA predictions to closer agreement with experiments and hand calculations.

5.5. Free Clip Test Setup

A schematic of the brace test frame is shown in Figure 69. It is designed such that the brace can be flipped over such that the face that is currently facing inwards will be facing outwards. In the alternate orientation the clip end will be above instead of below the root end. The load is applied by a hydraulic cylinder that is positioned such that it pulls vertically, applying the load in the opposite direction from the guided clip testing. The link between the load cell and the clip end is designed to eliminate restraining moments at the clip end. Load was measured with a load cell. Figure 69 shows specimen 4 mounted in the test frame post-test and after the load had been entirely relieved.

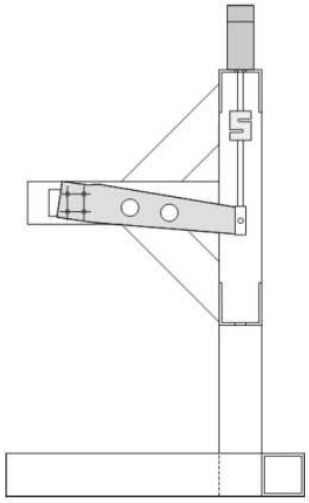

Figure 68: Brace Test Frame Schematic

Figure 69: Brace Test Frame

Each brace was mounted to the test frame with four Hi-Lok® fasteners at the root end. Each specimen was initially loaded to 1360 N (300 lbf) to remove slack from the connections then un-loaded. During every test one face was observed by DIC to measure displacements in the region of interest. In-plane strains were then calculated from these measured displacements. The specimens were loaded in small increments, 23 to 46 N (5 to10 lbf) when nearing failure, and at each load five DIC images were taken. The load from the load cell was also recorded concurrently with each image taken.

5.6. Free Clip Modeling

Only preliminary modeling of the brace with unconstrained clip end has been completed. Brace was modeled with 10 noded tetrahedral elements. The same mesh sizing was used as for the guided clip modeling in Section 5.2. Because the clip end was allowed to rotate, NX Nastran's implicit Advanced Nonlinear Solution (SOL 601) was used to analyze the models. The root was fixed using spider elements at each bolt hole, fixing only the three translational DOFs. The clip end was loaded by connecting the elements on the portion of the clip face shown in Figure 70 to the load application point using a rigid element. The load application point was located in the same location as in the experiments.

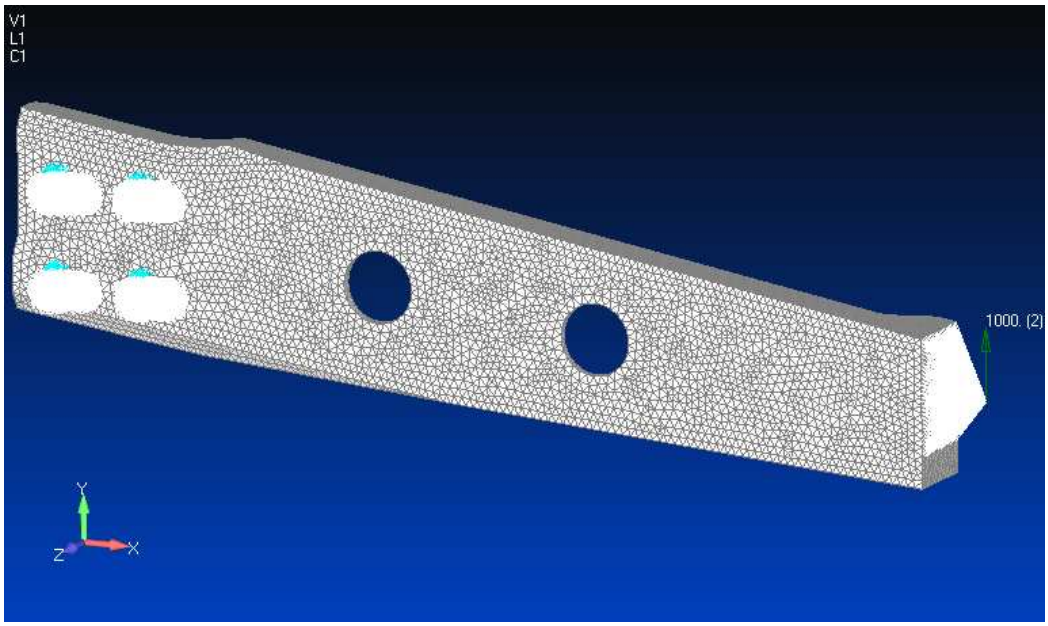

Figure 70: Meshed and Loaded Brace

5.7. Free Clip Experimental and Modeling Results

5.7.1. Testing Results

Six braces were tested. Load and strains were measured during each test. Load was measured using a load cell and strain was measured using both strain gauges and Digital Image Correlation (DIC). For three of the braces, the strain on the front face was observed using DIC and a strain gauge was mounted to both the upper and lower flanges. The loads recorded just prior to failure for all six specimens are listed in Table 23

Table 23: Brace Failure Loads

Specimen	Failure Load
Specimen 1	3.40 kN (764 lbf)
Specimen 2	3.60 kN (810 lbf)
Specimen 3	3.32 kN (746 lbf)
Specimen 4	3.71 kN (835 lbf)
Specimen 5	3.34 kN (750 lbf)
Specimen 6	2.89 kN (650 lbf)

Since loads were not recorded continuously as pressure was increased in the cylinder, actual failure load could be up to 46 N (10 lbf) higher than stated value. Figure 71 shows the DIC measurements of strain in the x direction, ε_{xx}, on the front face immediately pre and post failure for two of the tests. The two images have different scales for the contours, so the images are merely for comparison of strain patterns. The area of

maximum strain is indicated with the red arrows in both pre-failure images, and the failure location is indicated with the white arrows in both post-failure images. It can be seen that failure location was not indicated by a high strain region on the face of the specimen.

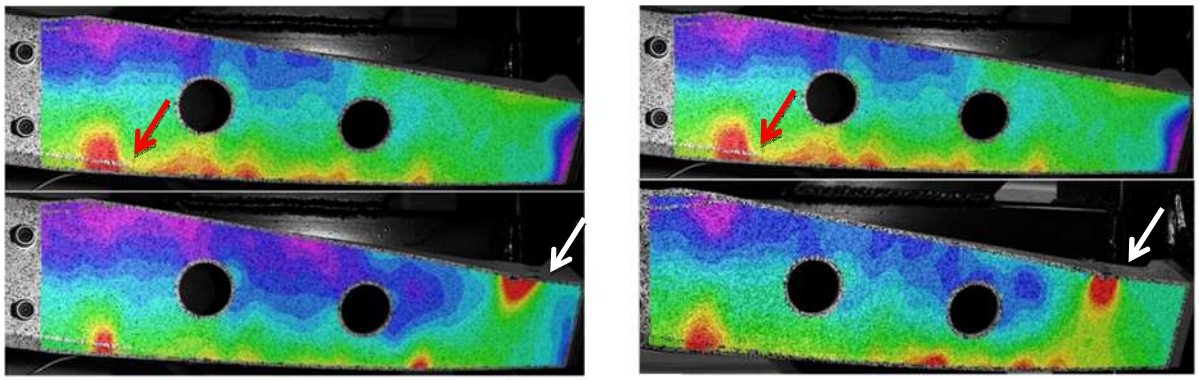

(a) Specimen 1 (b) Specimen 3

Figure 71: DIC Strain Measurements Pre/Post Failure

For specimen two, one strain gauge was also bonded to the same face observed with DIC to compare the DIC and strain gauge measurements. Figure 72 shows both the strain gauge measurement and the DIC measurement averaged over the strain gauge area for the test. Strain gauge data was lost at loads over 2730 kN (600 lbf) so only up to that load can be compared.

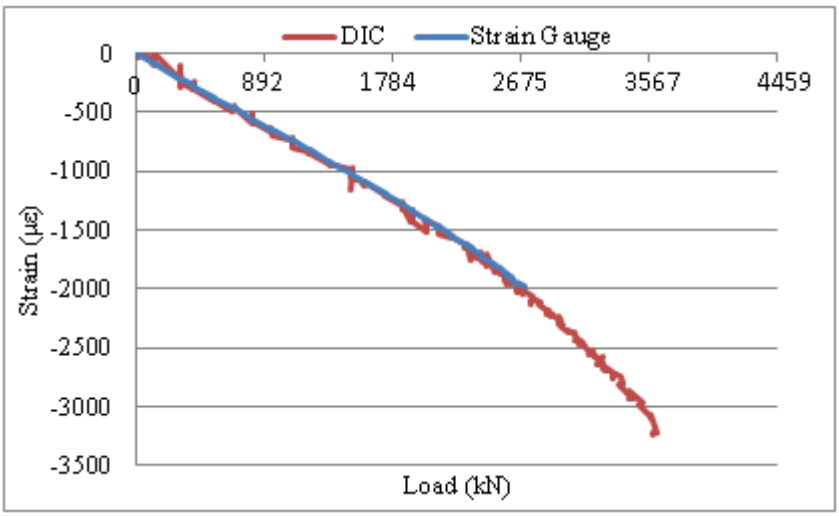

Figure 72: DIC to Strain Gauge Comparison

In order to compare the three specimens, the maximum and minimum strain in the x direction and the minimum shear strain at any point on the observed surface in each specimen were plotted together. The resulting plots are shown in Figures 73 through 75.

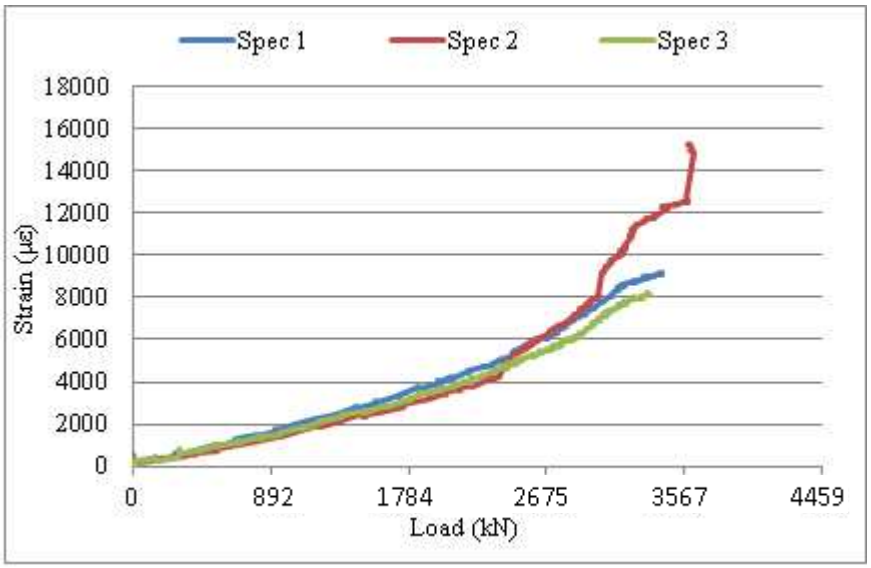

Figure 73: Maximum Axial Strain on Face

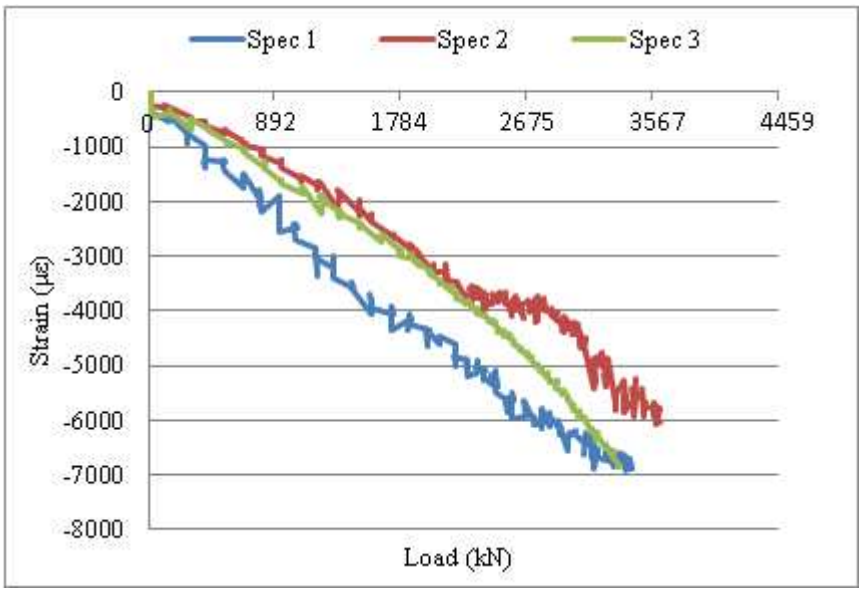

Figure 74: Minimum Axial Strain on Face

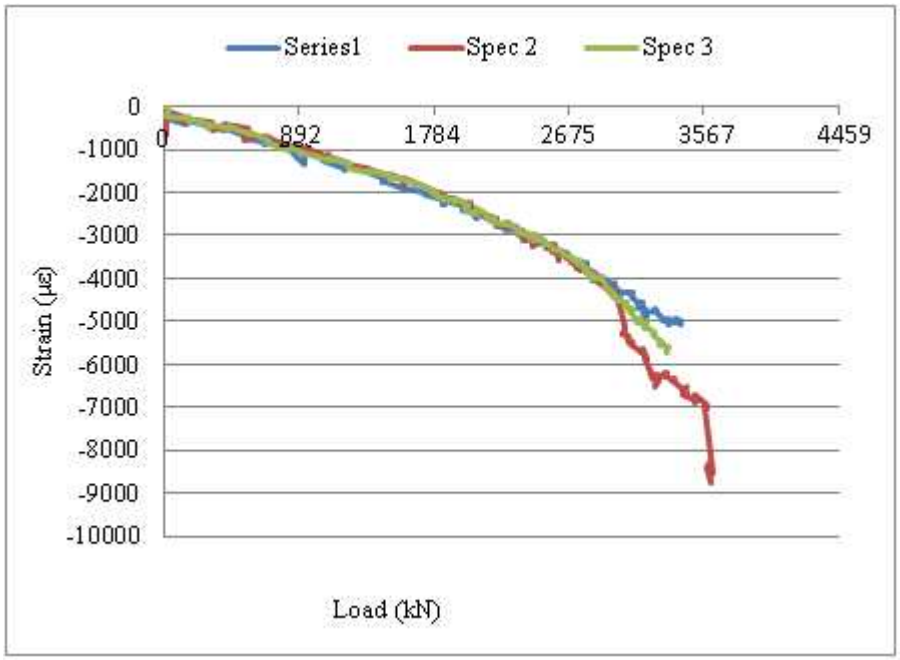

Figure 75: Minimum Shear Strain on Face

It can be seen that both the shear strain and the maximum tensile strain matches well for specimens 1 and 3. The comparison is less good for specimen 2. Inspection of specimen

2 and DIC data showed that there was actually localized failure in specimen 2 in the high strain region indicated in Figure 71. The change in behavior for the strains in specimen two corresponds with the localized failure in that high strain region. It is interesting to note however that despite the localized failure initiating about 1340 N (300 lbf) before substantial load drop, the final failure area is actually away from that region. Figure 76 shows surface evidence of the localized failure.

Figure 76: Spec 2 Surf Failure

The final three specimens were tested in the same configuration, but with the area of the top flange where failures occurred in the first three tests observed by the DIC. During one of the three tests failure occurred outside of the DIC field of view. The immediate pre and post failure images for all three tests are shown in Figures 77 through 79. It can clearly be seen that, for braces 4 and 6 failure occurred within the viewed region, at the point of

highest strain in the flange. However, specimen 5 did not fail at the location of highest strain in the viewed region, even though it experienced a higher strain than specimen 6. This disagreement suggests that using nominal strengths measured during coupon testing, may not be applicable for strength predictions when the stress field is not uniform, or complex stress states are experienced. It is important to note that because of the twisting of the clip end of the brace, it is not necessarily in a plane stress or strain state. At subsurface locations there is likely out-of-plane shear stress and strain among other factors that contribute to failure. DIC cannot be used to measure these quantities. It can be seen that strain data was lost on the right hand side of the viewed area in the tests of specimen 5 and 6. This was caused by rotation of the face such that reflections from lighting caused poor image quality for one of the cameras. This did not affect the other areas of the image.

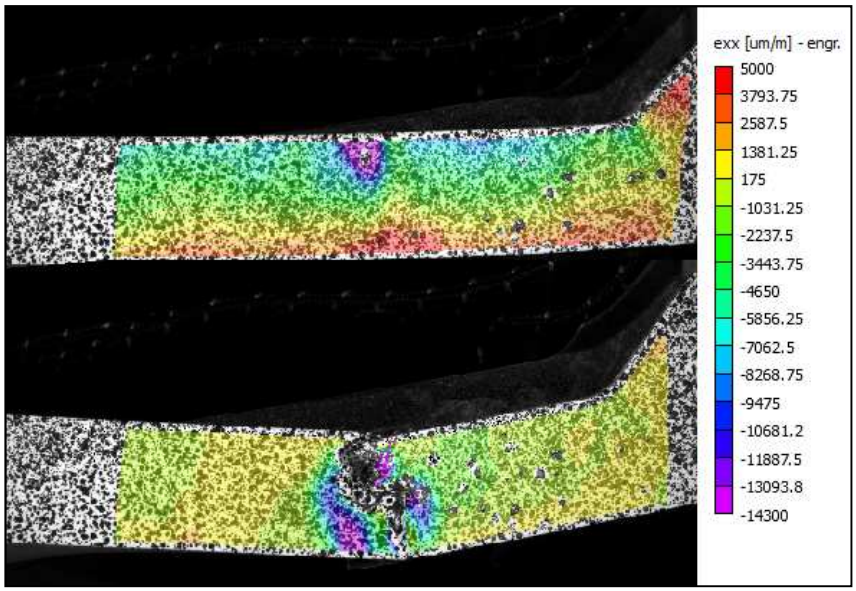

Figure 77: Specimen 4 Strain at Failure

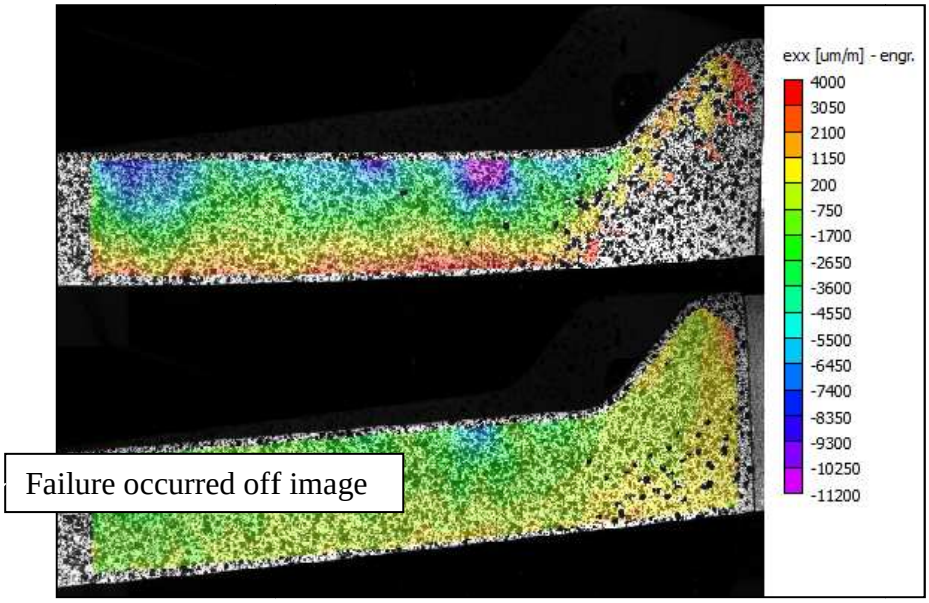

Figure 78: Spec 5 Strain at Failure

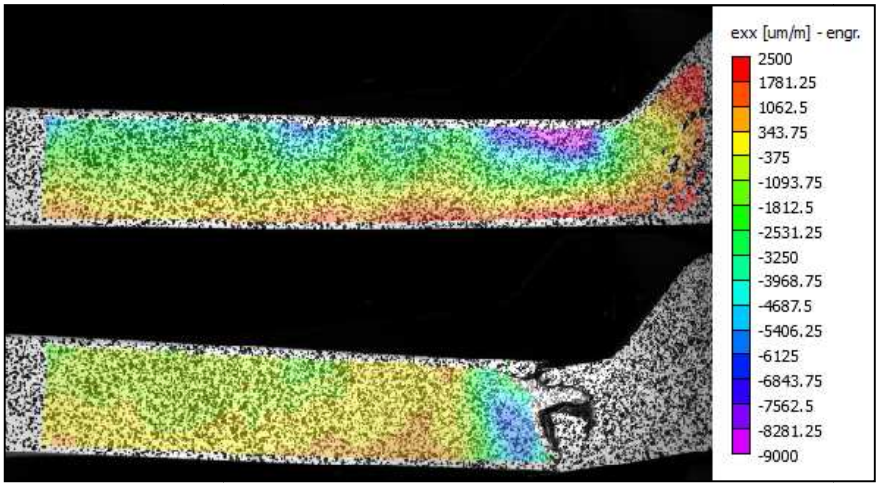

Figure 79: Specimen 6 Strain at Failure

Figure 80 shows a plot of the combined maximum strains measured for all six tests. It should be noted that the strains plotted as dotted lines represent compressive strains, in the plane of the top flange. The solid lines represent tensile strains in the plane of the face of the brace, measured during the first three tests.

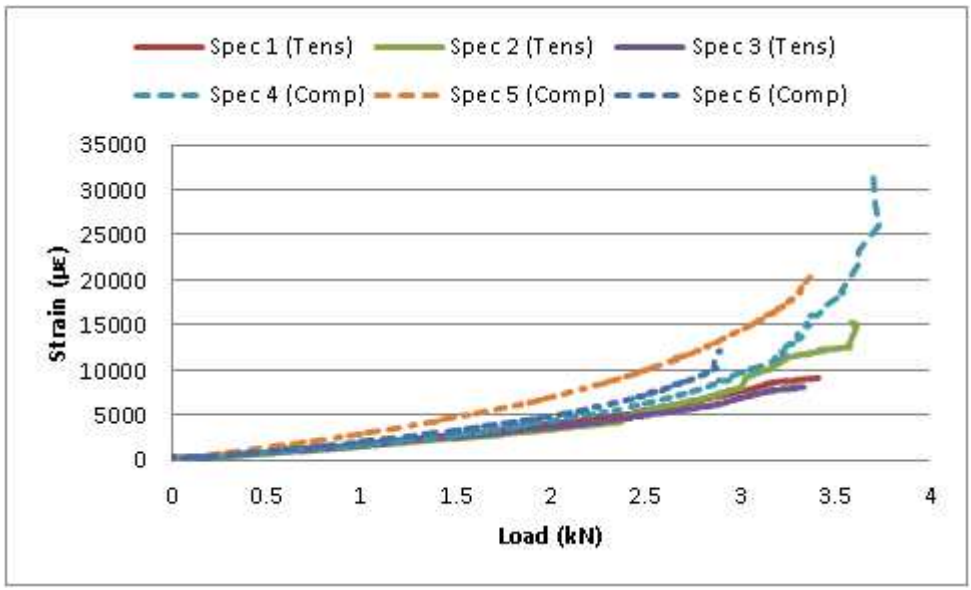

Figure 80: Highest Observed Strain

It is interesting to note that during initial loading, the strain in the two locations are roughly equal and opposite, the magnitude of the tensile strains on the face is roughly equal to the compressive strains in the top flange (with the exception of specimen 5, which did not fail at that region). However as the test progresses and the clip end twists under loading, the compressive strains in the top flange increase more quickly than the tensile strains on the face. By the time failure loads were reached, the compressive strains are at least 75% higher than the tensile strains at corresponding loads in the first three specimens. It is additionally interesting to note, that on the face, the highest tensile strain was consistently in the same location. In contrast, on the top flange the location of the maximum compressive strain varied greatly, with the failure locations occurring over a range of 120 mm (4.7 in). Additionally even when strains were very high on the face (as seen in specimen 2) final failure did not occur in that region, and in the case of specimen 5, strains on the top flange were extremely high, yet failure did not occur there. It was

seen during the testing presented in Section 4.1 that strains present on the surface of HexMC® are not necessarily present through the thickness. Due to the nature of the twisting experience by the brace, the region of high strain seen near the root was likely to be closer to uniaxial strain than was experienced by the region near the clip, where final failure finally occurred. Near the clip, the flange experienced twisting which certainly contributed to failure. Unfortunately as was discussed earlier, DIC cannot measure these out-of-plane shear strains. Additionally, it is quite likely that the additional thickness of the part in the region of the high tensile strains, prevented major damage from occurring.

5.7.2. Modeling Results

The predicted clip end rotations and displacements for the B-basis, average and B-max moduli in compression are compared to the first three specimens tested in Figure 81 and 82.

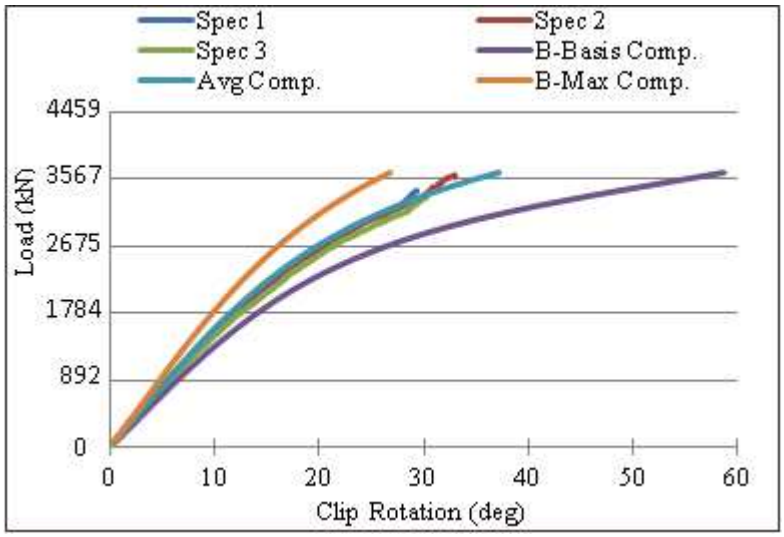

Figure 81: Clip End Rotation

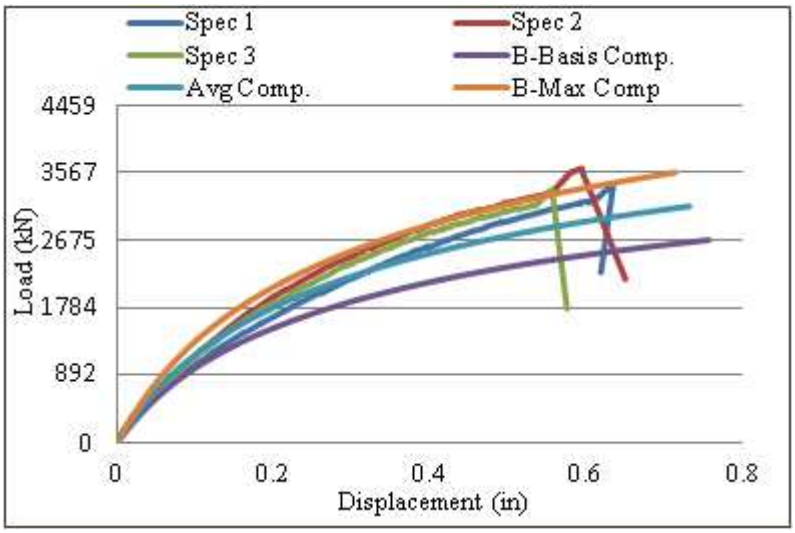

Figure 82: Clip End Total Displacement

It can be seen that both the total displacement and clip end rotation are well predicted. The strains were also decently predicted. Figure 83 shows the comparison of maximum principal strains predicted and measured on the front face of the brace. In the figures, the top image is the predicted strain contour, and the bottom three are the strain contours as measured using DIC. It can be seen that general qualitative agreement is fairly good on the shown surface.

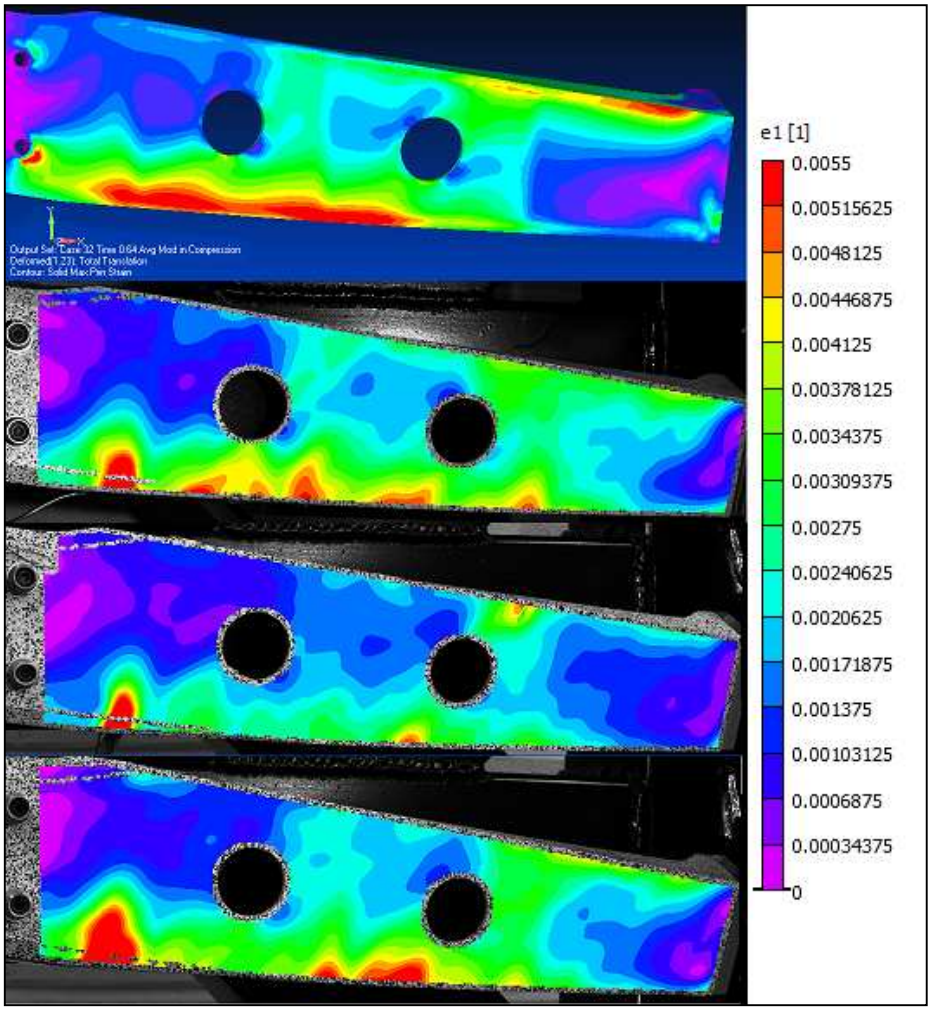

Figure 83: Max Principle Stresses

Figure 84 shows the axial strains predicted and measured near the failure region. All images are at near 650 lbs. It can be seen that general qualitative agreement is much poorer than seen on the front face. The region of high strain is not only much larger, but also greater in magnitude. It is also important to note that the strains are much higher than the failure strain predicted when the isotropic modulus and strengths that have been used are assumed. Using the assumed modulus and strength of 43.5 GPa (6.31 Msi) and 346 MPa (50.2 ksi), the failure strain should be near 8000 με.

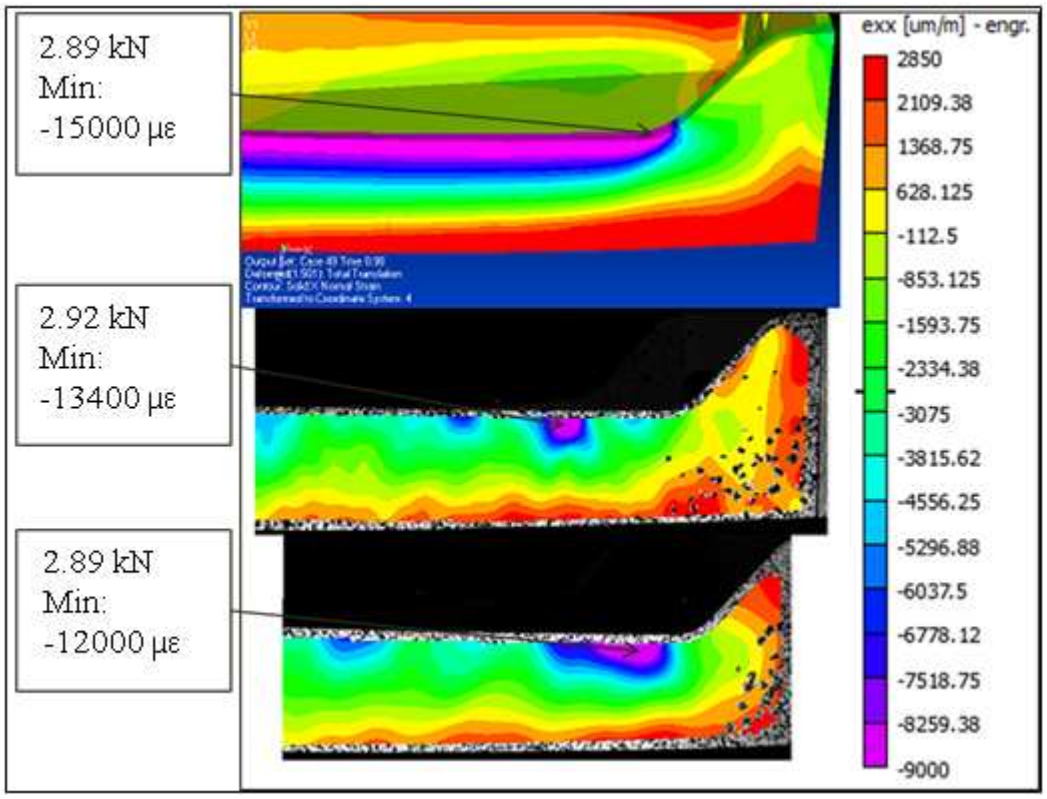

Figure 84: Strain near Failure Region

5.8. Free Clip Discussion

While incomplete the initial modeling efforts have shed light on improvements to the use of isotropic material properties for modeling. Displacements were well predicted, suggesting the moduli and boundary conditions are well modeled. The stresses predicted in the bolted regions were again much higher than those experience in reality, however it was shown in the guided clip modeling section that hand calculations provided the best predictions in these regions anyways.

Because of the non-linear nature of the loading in the unguided clip setup, this model would benefit from the use hexahedral elements. This would allow the application of in plane isotropic properties, allowing the transverse shear modulus to be lowered. This would likely improve both displacement and stress predictions.

Possibly the most important point this modeling raises however, is the problems associated with failure prediction in regions where high stress and strain gradients exist. The use of gross section stress to determine average strength from coupon tests provides a strength range which predicted failure fairly well in the case of the medium sized angle, and the guided clip brace testing, both situations where the stress state experienced by the material was fairly uniform near failure location. However in the unguided clip case, where fairly high gradients exist, the application of the gross section strengths becomes questionable.

6. Summary and Conclusions

This study focused on improving analysis methods used for predicting displacements and buckling loads of parts produced from HexMC®. Currently HexMC® parts must be certified for use in aircraft structures by large numbers of tested articles ("point design"), which is costly, time consuming and tends to lead to over designed parts. Because of this there is a desire to move towards certification by analysis supported by experiment. Toward this end, three tasks were set out for this study to address:

Task 1: Predict the buckling and failure loads of three sizes of HexMC® angle beams loaded in pure bending.

Task 2: Develop a stochastic modeling method that captures both the stiffness variation and membrane bending coupling effects exhibited by HexMC®.

Task 3: Predict displacements and failure loads of a HexMC® brace with complex geometry subjected to two different loading conditions.

6.1. Principal Results of the Study

- Pre-buckling behavior of HexMC® angle beams can be well predicted using a range of in-plane isotropic elastic properties. This study suggests that the B-basis to B-max moduli range presented here is a suitable range for in plane modulus. B range should be calculated using a suitably large sample size. B-basis modulus is calculated following a procedure similar to that used for calculation of B-basis strengths. B-max modulus should be calculated using similar procedure, but should be the top of the range, the modulus

under which 90% of specimens should fall 95% of the time. For buckling calculations, the elastic moduli in compression should be used, and the appropriate transverse shear properties should also be used.

- While the variation in buckling loads measured experimentally was captured by the B range moduli, the buckling loads of HexMC® angle beams were over predicted by 16 to 22% on average for the small and large angles. In addition, the post buckling behavior of the angles was not captured by the non-linear FEA analysis, with the tested angles exhibiting a more severe post buckling softening. This softening is suspected to be due to some progressive damage, as the stresses in the angle increase.
- The failure loads of the angles were over predicted by 18 to 32% for the small and large angles which buckled. For the medium size angles, which did not buckle, predicted failure loads were only 2-14% off. The reason for the large errors for the buckled angles is twofold. First, failure of buckled angles is dependent on the buckling load, which was over predicted. Second, the modeling did not predict the severity of the post buckled softening exhibited experimentally. The cumulative effect of these affects leads to large errors in failure prediction.
- For the selected RLVE size, stochastic RLVE modeling over predicted observed local strain variation, and slightly over predicted global strain variation. On average it captured variation well. Additionally it predicts the out-of-plane displacements seen experimentally, although exact comparisons are not possible because of difficulty in measuring the small out-of-plane displacements. Failure predictions using the RLVE method become difficult, because of the mesh dependency exhibited by the predicted ply

stress and strains. If the RLVE method is desired to be used for failure predictions, an area based criteria might be a possible approach.

- When the RLVE method was applied to the modeling of the angle beams, the variation in pre-buckling displacements exhibited by the angles was not captured by RLVE models. Despite this, buckling load predictions were improved for the small angle but not for the large angle size. This suggests that the proper RLVE size is dependent on multiple characteristic dimensions of the part being modeled, including thickness, and width.
- Failure loads of brace loaded with guided clip ends were able to be predicted to within about 15% when failure occurred away from bolted regions. Where the part failed in bolt bearing, hand calculations using reported stabilized bearing strength predicted failure load the best. Failures at the clip end, where failure was exhibited as peeling of the face of the clip, failure was not able to be adequately predicted using isotropic properties.
- Displacements and strains were well predicted for the brace tested with unguided clip end. Failure was not able to be well predicted however, as the strains both predicted and observed with DIC were approximately double than the failure strain predicted using the isotropic properties. This suggests that the nominal strengths obtained by tensile specimen can only be applied when the stress field is relatively uniform. When regions of high strain gradients exist, the nominal strengths cannot be used, because they under predict failure severely.

6.2. Future Needs

This work has shown the limitations of the methods discussed, and worked towards understanding the disparity between predictions and measurements. Initial work towards modeling the more complex geometry of the brace has been begun. Future work should continue a robust investigation into how well these methods work when applied to the braces, expanding the work already done to include modeling the material as an an-isotropic material. This will take into consideration the low transverse stiffness and shear modulus that HexMC® exhibits. Additionally, more testing should be conducted, in new loading conditions to access other modeling areas, if deemed necessary. Work should also continue towards failure predictions where stress and strain fields are severely non-uniform. This criterion could be an area based criteria and could be developed using more testing and the RLVE method.

References

[1] Boeing, "About the 787 Family," [Online]. Available: http://www.boeing.com/commercial/787family/background.html. [Accessed 5 March 2013].

[2] Boeing, "Boeing 787-8 Dreamliner: Fact Sheet," [Online]. Available: http://www.boeing.com/commercial/787family/787-8prod.html. [Accessed 5 March 2013].

[3] B. D. Agarwal, L. J. Broutman and K. Chandrashekhara, Analysis and Performance of Fiber Composits, Hoboken: John Wiley & Sons, Inc., 2006.

[4] J. C. Halpin, "Stiffness and Expansion Estimates for Oriented Short Fiber Composites," *Journal of Composite Materials,* vol. 3, no. October, pp. 732-734, 1969.

[5] J. C. Halpin and N. J. Pagano, "The Laminate Approximation for Randomly Oriented Fibrous Composites," *Journal of Composite Materials,* vol. 3, no. October, pp. 720-724, 1969.

[6] P. Feraboli, E. Peitso, T. Cleveland and P. B. Stickler, "Modulus Measurement for Prepreg-based Discontinuous Carbon Fiber/Epoxy Systems," *Journal of Composite Materials,* vol. 43, no. 19, pp. 1947-1965, 2009.

[7] P. Feraboli, E. Peitso, T. Cleveland, P. B. Stickler and J. C. Halpin, "Notched behaviour of prepreg-based discontinuous caron fiber/epoxy systems," *Composites:*

Part A, vol. 40, no. 3, pp. 289-299, 2009.

[8] NORDAM Group Inc., "Boeing 787 features composite window frames," *Reinforced Plastics,* vol. 51, no. 3, p. 4, March 2007.

[9] P. Feraboli, T. Cleveland, P. Stickler and J. Halpin, "Stochastic laminate analogy for simulating the variability in modulus of discontinuous composite materials," *Composite: Part A,* vol. 41, no. 4, pp. 557-570, 2010.

[10] P. Feraboli, E. Peitso, F. Deleo, T. Cleveland and P. B. Stickler, "Characterization of Prepreg-Based Desicontinuous Carbon Fiber/Epoxy Systems," *Journal of Reinforced Plastics and Composites,* vol. 28, no. 10, pp. 1191-1214, 2009.

[11] T. J. Shifman, Compression Molding Flow Effects on Material Properties for a Discontinuous Chipped FIber Composite, Seattle: University of Washington, 2001.

[12] M. Tuttle, "A Study of Structural Angle Beams Produced using Discontinuous-Fiber Composites," in *JAMS 2011 Technical Review*, San Diego, Ca, 2011.

[13] P. Feraboli and M. Ciccu, "Analysis method development for Discontinuous Compoiste Materials, part II," in *AMTAS Fall Meeting*, Edmonds Conference Center, 2010.

[14] M. A. Sutton, J.-J. Orteu and H. W. Schreier, Image Correlation for Shape, Motion and Deformation Measurements, New York: Springer Science+Business Media, LLC, 2009.

[15] B. Pan, "Study on Subset Size Selection in Digital Image Correlation for Speckle

Patterns," *Optics Express,* vol. 16, no. 10, pp. 7037-7048, 2008.

[16] The Hexcel Corporation, "AMTAS Test Report Allowable for HexMC Materials, Document No. HSTR 00006," The Hexcel Corporation, 2010.

[17] Siemens PLM Software, "NX Nastran 8 Help Library," 2011. [Online]. [Accessed 18 April 2013].

[18] The Hexcel Corporation, "8552R-AS4 Modulus Raw Data (AMTAS)," The Hexcel Corporation.

[19] U.S. Department of Defence, "Statistical Methods," in *Military Handbook Vol. 8: Polymer Matrix Composites Guidelines for Charecterization of Structural Materials*, p. Volume 1 Ch. 8.

[20] M. W. Hilburger and J. H. Starnes, "Effects of imprefections on the buckling response of compression-loaded composite shells," *International Journal of Non-Linear Mechanics,* vol. 37, no. 4-5, pp. 623-643, 2002.

[21] K. Marlett, "Hexcel 8552 AS4 Unidirectional Material Property Data Report," November 2011. [Online]. Available: http://www.niar.wichita.edu/coe/ncamphexcel.asp. [Accessed 2 April 2013].

[22] "Hi-Lok Fastening System," Hi-Shear Cormoration, [Online]. Available: http://www.hi-shear.com/fastener_hl_stds.htm. [Accessed 22 April 2013].

[23] The Hexcel Corporation, "Propriatary Hexcel Report," The Hexcel Corporation, 2009.